

Exploring specialization and sensitivity of convolutional neural networks in the context of simultaneous image augmentations

Pavel Kharyuk^{a,b,*}, Sergey Matveev^{c,a}, Ivan Oseledets^{d,b}

^a*Marchuk Institute of Numerical Mathematics, Gubkin str., 8, 119333, Moscow, Russia*

^b*Skolkovo Institute of Science and Technology, Bolshoy Boulevard, 30, p.1, 121205, Moscow, Russia*

^c*Faculty of Computational Mathematics and Cybernetics, Lomonosov Moscow State University, Leninskie gory, 1/52, 119991, Moscow, Russia*

^d*Artificial Intelligence Research Institute (AIRI), Moscow, Russia*

Abstract

Drawing parallels with the way biological networks are studied, we adapt the treatment–control paradigm to explainable artificial intelligence research and enrich it through multi-parametric input alterations. In this study, we propose a framework for investigating the internal inference impacted by input data augmentations. The internal changes in network operation are reflected in activation changes measured by variance, which can be decomposed into components related to each augmentation, employing Sobol indices and Shapley values. These quantities enable one to visualize sensitivity to different variables and use them for guided masking of activations. In addition, we introduce a way of single-class sensitivity analysis where the candidates are filtered according to their matching to prediction bias generated by targeted damaging of the activations. Relying on the observed parallels, we assume that the developed framework can potentially be transferred to studying biological neural networks in complex environments.

Keywords: explainable AI, Shapley values, Sobol indices, convolutional neural networks, sensitivity analysis, neural network specialization

1. Introduction

Deep neural networks are extensively used to solve a number of applied problems in various fields, such as computer vision [1, 2, 3, 4, 5], signal and audio processing [6, 7, 8, 9], natural language processing [10, 11, 12]. Being nonlinear multi-parametric models, they show efficient performance but are often employed as a black box. Numerous efforts to shed light on how these networks function have led to establishing an actively developing area of explainable artificial intelligence [13, 14], or XAI. Among methods developed for XAI are attribution methods, identifying the raw data components that mostly influence the network’s decision-making, and methods of constructing interpretable images that most activate its neurons. The latter include Activation Maximization [15], Deconvolutional Neural Networks [16], Network Inversion [17, 18], and Network dissection [19] approach (which may also be classified as an attribution method). Activation Maximization and visualization by Deconvolutional Neural Networks are designed to construct images to which the distinct neurons react most strongly. Network Inversion recovers input images by their feature maps from different layers, making it possible to understand which information from the original feature space is retained in each layer. The Network dissection method matches neurons with individual semantic parts of the original images. The capabilities of the methods have been demonstrated [20] in tasks of representation analysis in neural style transfer and visualization of adversarial noise and examples.

*Corresponding author

Email address: pavel.kharyuk@gmail.com (Pavel Kharyuk)

More than that, artificial neural networks have already extended beyond the abstract biologically inspired models built to solve classical machine learning problems. They are actively used as a proxy for neural coding and decoding of their biological origins. For example, internal activations of deep neural networks were successfully related to the neural activity in the auditory pathway, revealing the convergence between artificial model representations and the neurophysiological activity [21]. The evolution of the artificial models' capabilities means they can be studied by applying methods and paradigms established in neuroscience, particularly the treatment-control paradigm. Indeed, one may feed the specific inputs or distort the inference and measure the resulting changes in activations. Employing the single treatment, though, is restrictive. Thus, the series of multiple treatments considered simultaneously better matches the real-world conditions. Intentional modification to the input is known as augmentation. Since the visual data transformations can be traced and displayed most prominently, we are focused on analyzing the convolutional neural networks designed for image classification.

An important group of methods for studying data processing models is sensitivity analysis, which seeks to estimate the contribution of the degree of uncertainty of selected variables to the total uncertainty of the mapping. On the whole, sensitivity analysis belongs to a broader class of variable importance methods (VIMs). The corresponding variable importance analysis [22] includes difference-based VIMs, parametric and non-parametric regression techniques, hypothesis-test techniques, variance-based and moment-independent VIMs, and graphical VIMs. We pay special attention to the variance-based VIMs as the variance naturally incorporates both the firing specifics of the network's inference and the impact of input modifications (treatments). More specifically, such variance-based VIMs as Sobol indices [23] and Shapley values [24] decompose the variance into components related to the subsets of variables controlling the input augmentation.

Both sensitivity analysis methods and various visualization techniques are usually considered for low-level features, e.g., for distinct pixels. In our work, we considered the variance-based VIMs measuring the influence of the high-level variables, thus significantly reducing the feature space's dimensionality. Moreover, many artificial intelligence models do not directly relate to high-level concepts familiar or understandable to humans [25], which significantly complicates the analysis by means of low-level variables. As we worked with explicit computational models considering a limited number of fully controlled high-level variables in order to explore and hypothesize the possible connections between internal activations and treatments, our approach is minimally affected by the drawbacks of Sobol indices [22]. However, computing the Sobol indices in the case of the dependent variables is complicated by the additional consideration of the correlated parts. The Shapley values-based approach covers the issue automatically but has its own implementation difficulties. Lundberg et al. [26] have proposed options for the practical use of Shapley values as a method for sensitivity analysis of computational models, including a special case for linear models (Linear SHAP), methods with simplified computing of expectations (Low-order SHAP, Max SHAP), and DeepSHAP method combining DeepLIFT [27] approach and Shapley values. In addition, the authors have constructed a model-independent KernelSHAP method based on Linear LIME [28] (weighted least-squares between computational and linear explanation models) with Shapley values as weights.

Compared to certain existing explainability methods, we propose to focus on how the network propagates input distortions themselves instead of using them to build attribution maps for specific image samples (as, for instance, in [16, 28, 29, 30]). Although there are known studies that also explore the influence of various types of distortion [31, 32, 33, 34, 35], to the best of our knowledge, simultaneous input augmentations have not been presented yet. We see our main contribution as addressing this issue and proposing a framework that is able to account for potential dependencies among injected distortions, as well as for other variables affecting input data (such as class or data partition). As dependencies rise even from the non-permutability of the sequential augmentations, their order is another crucial factor incorporated into our analysis.

In this work, we have employed the sensitivity analysis based on Sobol indices and Shapley values for highlighting the network's components that give the most prominent feedback in response to the input augmentations. As a result, we introduce the framework of selecting and studying the units sensitive to the input data augmentations (Figure 1). The variables incorporated in the analysis are augmentation-related, augmentation-permuting, partition- and class-selecting ones. Computed values are plotted as sensitivity maps, which were investigated manually and used as features for correlational and linear discriminant

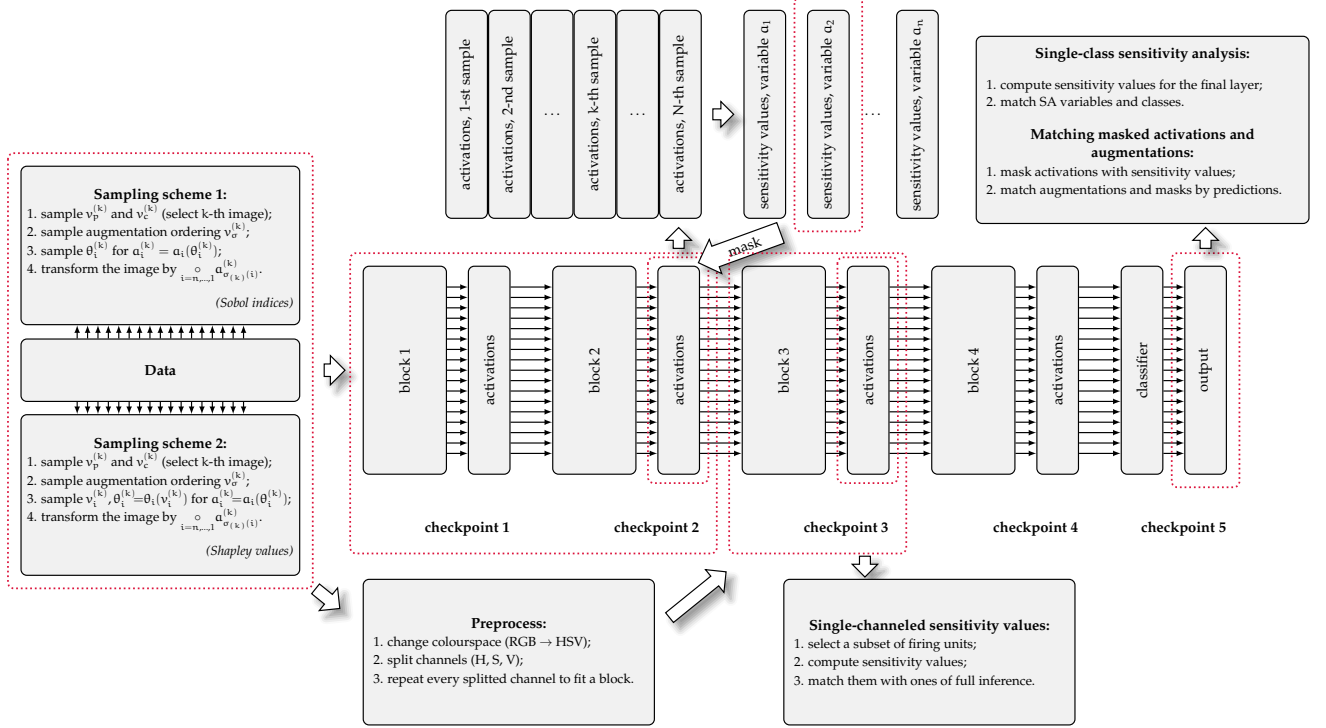


Figure 1: Summarized pipeline of the proposed framework. A block is referred to as a segment of a neural network participating in the analysis as a single mapping from its input to the corresponding activations. A checkpoint is a point of the network at which activations are gathered; as it is related to the preceding block, we use both terms interchangeably.

analysis. This analysis enabled us to identify internal neural processing tendencies layerwise and on a single unit scale, validated by damaging the convolutional checkpoints with a guided masking prediction as an independent procedure that matches sensitivity values with corresponding augmentations. In addition, we performed the single-class sensitivity analysis as an effort to understand the sensitivity of the whole network on the basis of the classifying layer sensitivity. As evidence that these findings are generalizable, we seek for prediction bias - more frequent prediction of the classes identified by the classifying layer as sensitive to an augmentation - generated by the guided masking of convolutional checkpoints. Finally, the framework was adapted to analyze the network segments. In the example of AlexNet [36], VGG11 [37], and ResNet18 [38] models, we demonstrate the alignment among different analysis blocks and consistency with the external knowledge, including patterns observed in biological circuits. We also recognize our findings as potentially transferable for studying biological neural networks in complex environments.

2. Materials and methods

2.1. Convolutional neural networks

By artificial neural network, we usually mean a parametric mapping with a layered structure, every single layer of which is a linear transformation of inputs followed by an element-wise nonlinearity. As an example, a feedforward network may be mentioned, $f(x) = l_N[l_{N-1}[\dots l_1[x]]]$, where $l_i[z] = g_i(W_i z + b_i)$ are layers, W_i - matrices of complementary sizes, b_i - bias vectors, $g_i(\cdot)$ - element-wise nonlinearities, $i = \overline{1, N}$. A layer is constituted by a combination of several individual “neurons”, mathematical models of the real biological neurons, which are parameterized by single rows of the matrix W and corresponding components of the bias vector b .

Convolution networks are artificial neural networks in which the linear part of the majority of layers is parameterized by convolutions, $W[x] : \mathbb{R}^{c_{\text{in}} \times n_1 \times \dots \times n_d} \rightarrow \mathbb{R}^{c_{\text{out}} \times m_1 \times \dots \times m_d}$,

$$y_{i,s_1,\dots,s_d} = \sum_j w_{i,j,\cdot} * x_{j,\cdot} = \sum_j \sum_{1 \leq k_1 \leq n_1} \dots \sum_{1 \leq k_d \leq n_d} w_{i,j,k_1,\dots,k_d} x_{j,s_1-k_1,\dots,s_d-k_d}, \quad (1)$$

$$w \in \mathbb{R}^{c_{\text{out}} \times c_{\text{in}} \times k_1 \times \dots \times k_d}, s_t = \overline{1, m_t}, t = \overline{1, d}.$$

In the equation above, we skipped the stride and dilation parameters for simplicity (by default, their values are 1 and 0 correspondingly). The stride parameter is responsible for the offset between neighbouring blocks transmitted to the convolution receptive field, and the dilation controls the offsets among elements to be associated as a single block. Non-strided and non-dilated layers of this type are shift-equivariant, meaning they can react on the target subvector (submatrix, subtensor) regardless of its position, and the corresponding activation will be only shifted. This property is similar to the visual system's ability to recognize sensed objects regardless of binding their position to a concrete visual field point. Among other parallels that could be drawn between convolutional layers and the human visual system, it is worth noting the following points: (1) the local connectivity of convolutional layers and the local connections between cells of the visual pathway (retina, lateral ganglion nucleus, striatum cortex) [39, 40], which define the presence of receptive fields; (2) the visual cortex organization, where beyond the primary visual cortex there are areas of processing the higher order visual information, and the primary visual cortex itself reacts on the low-level features like orientation or direction of local edges [39, 40], and the CNN layers' organization, where the deeper layer is, the more complex stimulus raise their reaction [16, 41]. From a computational point of view, the convolutional layers are also attractive because they have fewer parameters than fully-connected ones and thus require fewer computational resources for learning and inference.

For classification tasks, where an artificial neural network (ANN) is to be trained on some training set to recognize labels of input samples, variations of the following architecture are common. It begins as a pool of several convolutional layers, with a filter number growing with depth, followed by several fully-connected layers, the last of which has the number of outputs equal to the number of classes. Such architectures force the output to gradually decrease "physical" dimensionality and increase the number of channels. Real architectures also contain different submodules to improve the computational stability of learning (e.g., batch-norms), to prevent overfitting (like dropouts), etc.

Known architectures of such networks include AlexNet [36], VGG [37], ResNet [38]. One of the features of the last mentioned family is the presence of skip-connections, allowing such networks to reuse data representation from previous layers within deeper structures. Such property makes the ResNet-like networks closer to real biological neural networks (for example, in the visual cortex, there are $V1 \rightarrow V4$ and $V1 \rightarrow MT$ shortcuts in addition to $V1 \rightarrow V2 \rightarrow V4$ and $V1 \rightarrow V2 \rightarrow MT$ paths [40]).

2.2. Sobol indices

Sobol indices are utilized for sensitivity analysis and arise as values that describe the amount of variance explained by the different subsets of variables [23, 42]. Sensitivity analysis of this type requires a particular real-valued function that depends on several variables. Sobol indices are closely related to the ANOVA, allowing one to determine the proportion of variance in the mapping explained by a simultaneous change in a combination of several variables. In neural networks, a single neuron can constitute such a mapping.

Let x_1, \dots, x_d be a set of independent variables (factors), for which we consider a function $f : \mathbb{R}^d \rightarrow \mathbb{R}$. To avoid cluttering the indices within formulas, let us introduce the following designation, $\alpha = \{j_1, \dots, j_{|\alpha|}\} \subset D \equiv \{1, \dots, d\}$, where $|\alpha|$ is a number of elements in the set, and then we may denote a subset of variables w.r.t. α as $x_\alpha = (x_{j_1}, \dots, x_{j_{|\alpha|}})$. Let us also write the complement of α to the set D as $\bar{\alpha} = D \setminus \alpha$.

Taking into account Sobol's derivation and Hoeffding's decomposition [43] with the conditions $E_{x_\beta}[f_\alpha(x_\alpha)] = 0 \forall \beta \subset \alpha \subseteq D$, one can come to the following unique representation of such a function:

$$f(x_1, \dots, x_d) = \underbrace{f_0}_{\text{constant}} + \sum_{1 \leq i \leq d} \underbrace{f_i(x_i)}_{\text{major effect}} + \sum_{1 \leq i < j \leq d} \underbrace{f_{ij}(x_i, x_j)}_{\text{2nd-order effect}} + \dots = \sum_{0 \leq s \leq d} \sum_{\alpha: |\alpha|=s} f_\alpha(x_\alpha), \quad (2)$$

where the internal summands can be written as

$$\begin{aligned} f_0 &= E[f(x)], \quad f_i(x_i) = E_{x_{\overline{\{i\}}}}[f(x)|x_i] - f_0, \\ f_{ij}(x_i, x_j) &= E_{x_{\overline{\{i,j\}}}}[f(x)|x_i, x_j] - (f_0 + f_i(x_i) + f_j(x_j)), \quad \dots; \end{aligned} \quad (3)$$

and in the general case they can be found from the equations $f_\alpha(x_\alpha) = E_{x_{\overline{\alpha}}}[f(x)|x_\alpha] - \sum_{\beta \subsetneq \alpha} f_\beta(x_\beta)$. Moreover, using this decomposition, one may construct the following representation of the mapping's variance:

$$V[f(x)] = E[(f(x) - E[f(x)])^2] = \sum_{1 \leq i \leq d} V_i(f(x)) + \sum_{1 \leq i \leq d} \sum_{1 \leq i < j \leq d} V_{ij}(f(x)) + \dots = \sum_{\alpha \subseteq D} V_\alpha(f(x)), \quad (4)$$

with the partial variances $V_\alpha(f(x)) = V_{x_{\overline{\alpha}}}[f_\alpha(x_\alpha)]$. Hereby, the Sobol indices are defined as

$$\begin{aligned} S_\alpha(f(x)) &= \frac{\sum_{\beta \subseteq \alpha} V_\beta(f(x))}{V[f(x)]} = \frac{V_{x_\alpha}[E_{x_{\overline{\alpha}}}[f(x)|x_\alpha]]}{V[f(x)]}, \\ S_\alpha^T(f(x)) &= \frac{\sum_{|\alpha \cap \beta| > 0} V_\beta(f(x))}{V[f(x)]} = 1 - \frac{V_{x_{\overline{\alpha}}}[E_{x_\alpha}[f(x)|x_{\overline{\alpha}}]]}{V[f(x)]}, \end{aligned} \quad (5)$$

where $S_\alpha(f(x))$ is an ordinary Sobol index for a combination of variables α , and $S_\alpha^T(f(x))$ is the so-called total Sobol index for the same combination. The difference between them consists of the following: ordinary Sobol indices indicate the variance fraction explained by a single combination, whereas the total indices accumulate variance fractions of all variable combinations that contain the x_α within them. Total effect indices are used for many-variable cases to reduce the computational complexity. There is also the following relations between these indices: $0 \leq S_\alpha(f(x)) \leq S_\alpha^T(f(x)) \leq 1$.

In practice, Sobol indices are computed by sampling in a mapping domain. In this work, we employed the quasi-Monte-Carlo methods, Sobol sequencing [23], and Saltelli sampling [44] implemented in the SALib python package [45].

Finally, multiple variables may be grouped [46]. For example, if we consider the augmentation parameters as independent variables, we can combine them directly by belonging to a particular type of augmentation. Such grouping substantially facilitates further analysis, suggesting interactions between higher-level instances to be explored.

2.3. Shapley values

However, in the real scenario, the statistical independence of the variables is not necessarily satisfied. In this case, the variance decomposition ANOVA (4) is not valid. Its generalization, ANCOVA, with corresponding changes in the Sobol indices, is to be considered [47]:

$$V[f(x)] = \sum_{\alpha \subseteq D} \underbrace{\text{Cov}(f(x), f_\alpha(x_\alpha))}_{=V[f(x)] \cdot S_\alpha} = \sum_{\alpha \subseteq D} \left(\underbrace{V_\alpha[f(x)]}_{=V[f(x)] \cdot S_\alpha^u} + \underbrace{\text{Cov}(f_\alpha(x_\alpha), \sum_{\beta \subseteq \overline{\alpha}} f_\beta(x_\beta))}_{=V[f(x)] \cdot S_\alpha^c} \right), \quad (6)$$

where $\text{Cov}(z_1, z_2)$ is the covariance between z_1 and z_2 , S_α is the analogue of the standard Sobol indices, which are decomposed into the sum of the variance from uncorrelated, S_α^u , and correlated, S_α^c , contributions. There are several difficulties in constructing this type of decomposition [47, 48]. Another alternative is to reconsider the basic computational model as a fully probabilistic one expressed as a Bayesian network [49], however, it requires providing a statistical model of the input data, which is a separate challenging task.

The authors of article [24] have proposed an approach based on Shapley values, which they refer to as Shapley effects. The interpretation of Shapley values is the following: they are the contribution of each variable to the prediction averaged over different combinations of them. Assume, as before, that we have a set of variables $\{x_i\}_{i=1}^d$ for which we consider some cost (value) function $c : 2^d \rightarrow \mathbb{R}$, $c(\emptyset) = 0$ that determines the significance of the contribution of each combination of variables. Under these conditions, the Shapley value for a single variable is defined as

$$v_i = \sum_{\alpha \subseteq D \setminus \{i\}} w_\alpha (c(\alpha \cup \{i\}) - c(\alpha)), \quad w_\alpha = \frac{(d - |\alpha| - 1)! |\alpha|!}{d!} = \frac{1}{d} \left[C_{d-1}^{|\alpha|} \right]^{-1}. \quad (7)$$

The cost function should be chosen to relate the variables and their contribution to the total variance. These can be the numerators of the Sobol indices:

$$c_1(\alpha) = V_{x_\alpha} [E_{x_{\bar{\alpha}}} [f(x)|x_\alpha]], \quad c_T(\alpha) = V[f(x)] - V_{x_{\bar{\alpha}}} [E_{x_\alpha} [f(x)|x_{\bar{\alpha}}]] = E_{x_{\bar{\alpha}}} [V_{x_\alpha} [f(x)|x_{\bar{\alpha}}]], \quad (8)$$

and the article [24] shows that the selection of these cost functions results in the equivalent Shapley values; however, as the authors noted, in practice $c_T(\alpha)$ is preferable when used within the Monte-Carlo estimator. An essential feature of Shapley values determined in this way is that they always sum to the total variance.

For practical computation, the formula (7) can be rewritten through permutations of the variables as

$$v_i = \sum_{\pi \in \Pi(D)} \frac{1}{d!} (c(P_i(\pi) \cup \{i\}) - c(P_i(\pi))), \quad (9)$$

where $\Pi(D)$ is the set of all $d!$ permutations of variables from D , $P_i(\pi) = \{\pi(1), \dots, \pi(j)|\pi(j+1) = i\}$ are the variables in the permutation π preceding the i -th one. To calculate this value, the authors [24] used approximation by sampling a subset of possible permutations, followed by averaging.

2.4. Data augmentation

Data augmentation refers to various transformations made to increase the training samples' size and population. Moderate augmentation allows the neural network to "observe" more diverse examples, acting as a regularizer to reduce overfitting. Augmentation is used both for small sample problems and improving learning stability on large datasets [50] - the article's authors fairly compare augmentation with dreaming, one of the essential human mental functions.

Following the authors [50], existing augmentation methods can be roughly divided into warping (transforming existing samples) and oversampling (generating new ones). In the imaging domain, the following examples of warping were pointed out: various geometric transformations reducing positional/translational bias, colour space (photometric) transformations minimizing lighting biases, different kinds of blurring which enhance resistance to motion blur, cropping which addresses the scaling variability, random erasing making a network more resistant for occlusion (unclear parts of images) and suppressing the subset-oriented learning, when the most of original feature space is ignored. Oversampling methods are aimed at the estimation of data distribution and include k-Nearest Neighbours (k-NN) interpolation, guided data learning with generative-adversarial networks (GAN), neural style transfer, which allows one to switch between high-level parameters of data (such as day/night, winter/summer, artist style, etc.).

The application of particular augmentation methods requires many conditions to be considered. First, there must be some prior knowledge about the nature of the data, with which new samples must comply. For example, the typical camera orientation makes it meaningless to reflect images vertically. The second is limiting the number of new samples. In particular, excessive augmentation on small samples suppresses true variability in the data since it is difficult to account for all possible sources of variance on a small sample number. In addition, augmentation should not significantly distort or skew the true distribution of the data in another way; otherwise, we again encounter the overfitting problem.

2.4.1. Sampling schemes and variables for sensitivity analysis.

Data augmentation causes changes in the pattern of neuronal activations. It seems natural to assume that some kind of specialization, similar to one in biological neurons, can be established among all neurons in the network. We can assume such a specialization both at the level of single neurons (like single neurons in the inferior temporal cortex, which are involved in face/hand/facial expression recognition [40]) and at the level of their groups (e.g., as regional cerebral blood flow increase in V4 during representation of coloured abstract figures or V5/MT activation in response to visual moving patterns [40, 51]). In this work, we propose to use augmentation transformations within the network sensitivity analysis to test these

assumptions; as a first step, we have focused on warping, and hereinafter, we will refer to the latter as augmentations. Each transformation is defined by its own set of parameters θ_i , $i = \overline{1, d}$, which are treated as variables. Augmentations without inner parameters (e.g., horizontal flip) are supplied with the switching parameter, deciding whether to apply a transformation. In addition, the model of input space is extended with a categorical class variable $v_c \sim \text{Cat}(1, \dots, C)$. Considering separate variables for each class would give more freedom in the analysis but would also significantly increase the dimensionality of input space, making the approach impractical.

Furthermore, we added another auxiliary variable related to the dataset partition. Input data is generally divided into non-intersecting training and validation subsets. An ANN is trained using the first part, and the second partition is utilized for tuning the network's hyperparameters and other testing. The corresponding independent variable in our analysis is $v_p \sim \text{Cat}(\{\text{train}, \text{valid}\})$, $p(v_p = \text{train}) = p(v_p = \text{valid}) = 1/2$.

The critical thing to note is that successive transformations over data are generally not permutable. As an example, it is sufficient to consider the following pair: $g_1(\cdot | \alpha)$ rotates the image by an angle α , $g_2(\cdot | \theta_{g_2})$ fills with zeros some rectangular region of the image specified by a set of parameters θ_{g_2} , - obviously, $g_1(g_2(\cdot | \theta_{g_2}) | \alpha) \neq g_2(g_1(\cdot | \alpha) | \theta_{g_2})$. Therefore, to account for the transformations ordering, in addition to the variables $\{\theta_i\}_{i=1}^d$ corresponding directly to their parameters, we introduced a separate variable $v_\sigma \sim \text{Cat}(\Pi(D))$, $p(v_\sigma = \widehat{v_\sigma}) = 1/d!$ whose realization with equal probability determines one of the possible permutations of the d transformations:

$$p(v_c, v_p, v_\sigma, \theta_1, \dots, \theta_d) = p(v_c)p(v_p)p(v_\sigma) \prod_{i=1}^d p(\theta_i), \quad (10)$$

- in this case, all variables remain independent, and one can use the ANOVA model. It should also be noted that the number of possible permutations is reducible if some combinations of transformations are invariant to order.

Since each transformation modifies the data, the total number of transformations and their order are crucial. The samples obtained by applying too many transformations over the original data will likely lose representativeness. To address this issue, we supplemented the probabilistic model of input space with switching variables, $\{\gamma_i\}_{i=1}^d$, which indicate whether a transformation is applied. If a transformation is ignored, $\gamma_i = 0$, this situation can be viewed as applying a transformation with a set of parameters $\theta_{i,0}$, which turns it into an identical transformation, $g_i(\cdot | \theta_i = \theta_{i,0}) \equiv \text{id}$. The corresponding probabilistic model takes the form known as spike-and-slab [52]:

$$p(v_c, v_p, v_\sigma, v_1, \theta_1, \dots, v_d, \theta_d) = p(v_c)p(v_p)p(v_\sigma) \prod_{i=1}^d p(v_i, \theta_i), \quad (11)$$

$$p(v_i, \theta_i) = (1 - \gamma_i)p_0(\theta_i) + \gamma_i p(\theta_i), \quad p_0(\theta_i) = \delta(\theta - \theta_{i,0}), \quad \gamma_i = \mathbb{I}_{v_i > \tau_i}, \quad v_i \sim U[0, 1],$$

where γ_i is parameterized using uniformly distributed v_i , $0 < \tau_i < 1$ is a threshold specifying the probability of ignoring the transform, θ_i are the transformation parameters, and $\delta(\theta - \theta_{i,0})$ is the delta (point mass) distribution, $i = \overline{1, d}$. In this formulation, independence between the variables is lost: the parameters of each augmentation depend on the switching variables. This fact makes the results derived from the ANOVA model unreliable. However, Shapley values naturally account for the dependent case.

2.4.2. Augmentation sets.

Two separate sets of augmentations are considered (Figure 2): the A_1 set includes 5 transforms, $(A_{1.1})$ erase rectangular part of an image, $(A_{1.2})$ adjust sharpness by a fixed factor (1.5), $(A_{1.3})$ 2D rolling of pixels, $(A_{1.4})$ converting to grayscale, $(A_{1.5})$ Gaussian blurring; the A_2 set consists of $(A_{2.1})$ adjust brightness, $(A_{2.2})$ contrast, $(A_{2.3})$ saturation, $(A_{2.4})$ hue, $(A_{2.5})$ horizontal flip, $(A_{2.6})$ rotate image with successive cropping, $(A_{2.7})$ blur the random elliptic region of image. The non-augmented (original) data is denoted as A_0 .

2.4.3. Sensitivity analysis (SA) variables.

We refer to the variables θ_i (or v_i, θ_i in the (11) case) merged by corresponding augmentations, as well as auxiliary variables v_c, v_p, v_σ , as sensitivity analysis (SA) variables. All the θ_i variables and constant



Figure 2: Sample image from the ILSVRC dataset, its corresponding HSV decomposition and examples of single and simultaneous augmentations considered in the study.

parameters are listed in Table A.1.

2.5. Experimental setup

The computations are divided into three experimental series: (1) computing sensitivity values for components of networks by using augmented data as input to the first layer; (2) damaging activations using the sensitivity values; (3) calculating sensitivity values for selected neurons of standalone segments using single channels of original data represented in HSV format. For the first and the third experimental series, number of activations and number of samples are described in [Appendix A](#). Details related to the second series are provided below (2.5.2).

2.5.1. Full-scale sensitivity analysis.

The first experimental series is designed as follows. We select a set of submodules for each network to observe their activations (outputs). Hereinafter, we call them checkpoints and refer to them as either convolutional or fully-connected if the last linear mapping before measuring their activations is convolutional or fully-connected, respectively. During the experiment, data augmented by A_k , $k \in \{0, 1, 2\}$ are fed to the input layer. The resulting activations of the selected checkpoints are saved for subsequently calculating sensitivity values.

In the case of Sobol indices, we used the first feature space model (10), i.e. sequentially applied all augmentations given their permutation sampled. Variables corresponding to the inner parameters (for example, rotation angle, size and centre coordinates for rectangular erasing, etc.) are considered to be uniformly distributed on the specified intervals and sampled by the semi-random Sobol-Salteli method implemented in SALib [45].

The second input space model (11) designed for Shapley values includes nominal variables. To sample from such distribution, at first, we, similarly to the authors of the work [53], draw independent samples of the nominal variables, responsible for whether to apply transform or not. As all the resting variables have no dependence structure, we choose their default values (no augmentation) or sample them from corresponding marginals.

Computed sensitivity values (Figures S1–S6) were visually inspected and analyzed via extracting correlation and prediction patterns. The correlation patterns were evaluated by calculating unit-wise Spearman correlations between SA variables (Figures S7.2). Both augmentation sets were simultaneously considered in order to relate them. Units (output channels) of the fixed checkpoint were treated as observations. In the case of convolutional checkpoints, the results were spatially averaged. In addition to resulting correlation matrices, spatial correlation maps were generated to reflect the possible relationships between sensitivity to augmentations and coefficients of variations as a measure of unit activity (Figures S7.3).

Additional exploratory analysis was performed by extracting prediction patterns from confusion matrices (Figures S7.4). A convolutional neuron maps a multi-channelled image to a single-channelled one with sensitivity values to different SA variables assigned to each point. They were employed as features for predicting the SA variables. Resulting confusion matrices highlight high-level relationships between SA variables regarding linear separability patterns. As a separation method, we used cross-validated linear discriminant analysis (LDA): all units from a fixed convolutional checkpoint were split into training and validation sets by applying the K-fold scheme ($k = 5$) 100 times. Predictions were measured on the validation parts, and corresponding confusion matrices were computed as averages.

2.5.2. Masked activation analysis.

Sensitivity analysis assigns a variability level of activations in response to an applied augmentation to feature maps. The resulting “markup” may be employed as a mask outlining more and less sensitive areas, enabling guided editing of the activations. Such perturbations break the communication pathways established among neurons from neighbouring layers. It resembles a manual blocking (or activating) sensitive receptors located in the synaptic terminal, changing the chemical context while leaving the location of synapses and neurons unchanged, i.e., a variant of reversible brain damage, similar to the temporary effect caused by injecting a specific drug. The same idea stands behind the Dropout regularizing method, with the distinction that the latter completely zeroes out a subset of the output during the learning procedure.

Besides, there is a masking-based technique to estimate the sensitivity of occlusion attribution (e.g., [29]), where masking is applied as a single transformation to identify specific areas of an input exerting the strongest influence on the prediction. Recall that in our work we directly use the intermediate changes of activations derived from different combinations of various input augmentations. Sensitivity values allows one to assess the contribution of every SA variable to the activations’ variance. But how specific are the resulting sensitivity maps? Figure 3 demonstrates that sensitivity to several SA variables yields a compensatory effect for others. Moreover, there are intersections of augmentation actions, e.g., modifying the high-level feature like luminosity or sharpness. Therefore, the objective of the masked activation analysis comprises an integral specificity assessment of the sensitivity maps produced during simultaneous augmenting setup through matching them with single augmentations. Activation editing should not be mistaken with input augmentations: the latters are performed independently on any sensitivity maps, and activations within selected convolutional checkpoints are to be masked according to estimated sensitivity maps.

The current series’ experiments involve such editing to capture the changes in classification quality. The following masking approaches were used: raw values, inverted values (1 - value), and thresholded versions of the raw values, $\text{thr}_{\alpha,q}(x) = \alpha x \cdot \mathbb{I}_{x \in q-\text{quant.}} + x \cdot \mathbb{I}_{x \notin q-\text{quant.}}$, where $\alpha \geq 0$ is a gain ($\alpha > 1$) or damping ($0 \leq \alpha < 1$) factor, \mathbb{I}_A is an indicator of event A , $q - \text{quant.}$ is the q -th quantile of all current sensitivity values at the corresponding checkpoint; in this work $\alpha \in \{0, 0.5, 1.5\}$, $q \in \{0.5, 0.6, 0.7, 0.8, 0.9\}$.

The top-1 accuracy values measured for different masks form a new feature space for further analysis. These features were extracted for original input, as well as for augmented ones by every single augmentation considered in the study. Then, the special correlation matrices were constructed as tables with rows corresponding to augmentations of input and columns standing for SA variables used for masking (Figure 4). Each entry is a value of Spearman correlation between masked non-augmented input and input augmented by the same transform used for masking. Further reasoning is based on the assumption that computed sensitivity values are relevant to the real sensitivity to the corresponding augmentation, and matching the sources of distortion should lead to a larger deviation from the masked but non-augmented baseline, which may be reflected by decreasing the corresponding correlation value. Since the last fully-connected layer

decides the final prediction, it was excluded from the masking procedure (as well as other fully-connected checkpoints in the case of AlexNet and VGG11).

While investigating the sensitivity values, we observed them as skewed and non-uniform. Thus, we considered a problem of detecting the single-class sensitivity. The first-order Sobol indices and Shapley values were engaged to address this problem. Total Sobol indices were excluded from the consideration due to their weaker specificity. The candidate list may be ranked by a simple sorting in descending order of the sensitivity values. However, where to put a threshold separating the non-sensitive classes is not apparent. Our work employed a top-5 approach as a rule of thumb (Tables 2, 3). Using the same masking approach, we created a new pattern based on top-5 predictions to filter the results. Predictions and sensitive classes were matched between each other by the Jaccard index, which increases as predictions become more biased towards the sensitive classes (Tables 5, S7.6).

2.5.3. Cutting off the subnetworks and matching single-channel sensitivity on selected units.

In the last experimental series, we feed the data directly to the standalone segments of neighbouring checkpoints. As the number of input channels does not match the input data, we represented original images in HSV format (see Figure 2) and separately repeated each of the resulting channels to fit the corresponding segment (single-channel checkpoint). Then, we extracted the pixel-wise correlation patterns for different components of HSV decomposition with the original values from the first experimental series on the same manually generated subset of units recognized as the most sensitive to at least one of the augmentations (Figures S7.7). These experiments were conducted only on AlexNet and ResNet18.

The initial purpose of this analysis is to examine how well patterns extracted for isolated segments can be matched with the same patterns for a normally operating network. Computed correlational matrices may be related to each other to reveal higher-level patterns, showing how single-channel checkpoints differ by these correlations and how close they are to the original ones. These higher-level tendencies were extracted by treating the correlations as new feature space and computing the higher-level correlations on their basis (Figure 5).

3. Results

As a baseline, we measured the prediction accuracy for both augmentation sets, A_1 and A_2 , and compared them with results computed for the original data, A_0 (Table 1). These computations were performed on the validation partition; in the case of parameterized augmentations, a set of parameters was sampled three times for each data item. All the networks considered reveal that accuracy values change (decrease) unequally in response to the transformation. The most significant loss in accuracy is related to colour space alterations (hue, grayscale) and complete information removal (erasing). Augmentations that distort the input slightly have the lowest impact on the final score (horizontal flipping, local elliptic blurring, constant sharpness adjustment).

3.1. Accessing neuronal activation sensitivity with Sobol indices and Shapley values

The major results of this section are represented in Supplementary Figures S1–S6.

3.1.1. SA: total variances

Before studying the sensitivity values, indicating proportional variable contribution, we explore variances and coefficients of variation. As shown in Figures S7.1.1–S7.1.5, (a)–(b), distribution patterns for variances are similar for both sampling schemes and vary depending on the augmentation set. Since zero value of activations means zero contribution during inference, we considered the coefficient of variation (CoV) as a ratio of standard deviation to the absolute value of means to compare units directly (Figures S7.1.1–S7.1.5, (c)–(d)). They tend to be more uniform and more deviated from zero on the whole, suggesting that most units are involved in inference. No connection can be drawn between the units most sensitive to a single augmentation and those with high variances or CoVs (Figures S7.1.1–S7.1.5, Figures S1–S6, Figure 3).

Table 1: Accuracy scores for considered networks measured on the validation part of the corresponding dataset. All augmentations were applied independently as single transformations. In the case of parameterized augmentations, each image was used 3 times with different sets of sampled parameters.

Part A. Augmentation set 1.							
		(A ₀) Orig.	(A _{1.1}) Erasing	(A _{1.2}) Sharp.	(A _{1.3}) Rolling	(A _{1.4}) Grayscale	(A _{1.5}) Gaus.blur
<i>Imagenet (ILSVRC)</i>							
AlexNet	<i>top-1</i>	0.5631	0.3969	0.5588	0.5036	0.3395	0.4511
	<i>top-5</i>	0.7895	0.6269	0.7866	0.7413	0.5767	0.6927
VGG11	<i>top-1</i>	0.6888	0.5874	0.6862	0.6519	0.5497	0.5802
	<i>top-5</i>	0.8854	0.8106	0.8843	0.862	0.7926	0.8102
ResNet18	<i>top-1</i>	0.6967	0.5707	0.6937	0.6594	0.5589	0.6187
	<i>top-5</i>	0.89	0.7932	0.8901	0.8657	0.8004	0.8363
<i>Places 365</i>							
AlexNet	<i>top-1</i>	0.473	0.3288	0.4619	0.3934	0.2856	0.4056
	<i>top-5</i>	0.7776	0.6179	0.7698	0.7001	0.5594	0.7081
ResNet18	<i>top-1</i>	0.535	0.4411	0.5235	0.494	0.4209	0.4783
	<i>top-5</i>	0.8363	0.7544	0.8274	0.8015	0.729	0.7894

Part B. Augmentation set 2.							
		(A ₀) Orig.	(A _{2.1}) Bright.	(A _{2.2}) Contrast.	(A _{2.3}) Satur.	(A _{2.4}) Hue	(A _{2.5}) Hflip
<i>Imagenet (ILSVRC)</i>							
AlexNet	<i>top-1</i>	0.5631	0.496	0.4627	0.47	0.3392	0.5622
	<i>top-5</i>	0.7895	0.7265	0.6976	0.7114	0.5649	0.79
VGG11	<i>top-1</i>	0.6888	0.6253	0.5969	0.6323	0.5164	0.6879
	<i>top-5</i>	0.8854	0.8354	0.8184	0.8528	0.7581	0.8856
ResNet18	<i>top-1</i>	0.6967	0.6402	0.6163	0.6537	0.5534	0.6962
	<i>top-5</i>	0.89	0.8471	0.8322	0.8658	0.7914	0.8909
<i>Places 365</i>							
AlexNet	<i>top-1</i>	0.473	0.4122	0.3951	0.3969	0.2967	0.4729
	<i>top-5</i>	0.7776	0.7121	0.693	0.7008	0.5641	0.7784
ResNet18	<i>top-1</i>	0.535	0.4826	0.4581	0.4915	0.4184	0.533
	<i>top-5</i>	0.8363	0.7857	0.7641	0.8001	0.7233	0.835

The exception is AlexNet trained on the Places 365 dataset, where many neurons of the second, third and partially first checkpoints are inactive (Figures S7.1.4). As the network was trained from a scratch [54] (see also a link from [Data availability](#)), an improper weights initialization could cause the outcome. This issue impacts all further steps of our analysis (hereafter, we omit the remark), providing additional data on the framework’s robustness. ResNet18 did not surface the problem, presumably due to its skip-connection feature. Apart from that, we observed the similar tendencies as for ILSVRC.

3.1.2. SA: neuronal activation patterns

In general, considered sensitivity values complement each other. For example, the first-order Sobol indices highlight sensitivity to a single variable, and for some units it is hard to trace sensitivity to an elliptic local blur variable in this sense, while total Sobol indices capture all its interactions and display the blob-affected patterns, for all other variables included in the augmentation set. Similarly, Shapley values capture the same interference resulting in elliptic blob patterns but are limited by partition to unity constraint. In addition, the elliptic local blur variable also confirms that sensitivity to input changes may last up to deeper layers. Such sensitivity to transformations may affect either whole or certain neurons from a checkpoint, and the latter may support the existence of specialized structures. In Figure 3, (a)–(c), several examples of such

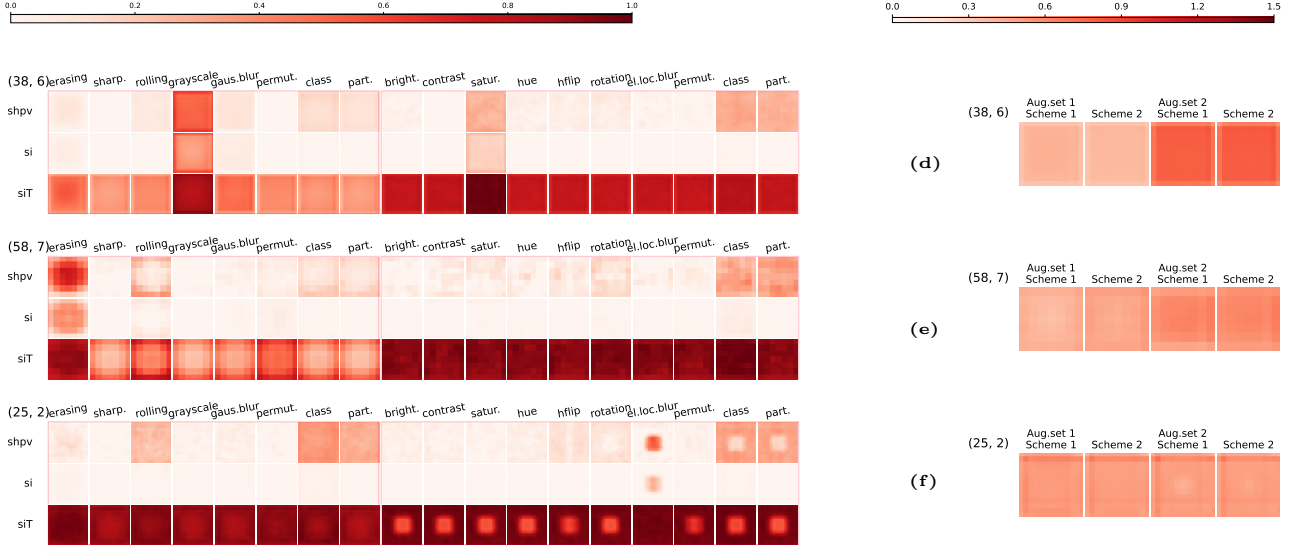


Figure 3: Examples of the sensitivity to initial augmentations of the ILSVRC input manifesting itself in deep layers (a–c) and corresponding log-transformed coefficients of variance (d–f). (a), (d): AlexNet, checkpoint at output from features.7 module, 301-st output channel (neuron), grayscale and saturation. The larger sensitivity to grayscaling matched with lower CoV value, and vice versa for saturation; (b), (e): VGG11, avgpool, 462, erasing. The prominent sensitivity to erasing is not expressed in higher CoV values; (c), (f): ResNet18, layer3, 193, rolling and elliptic local blur. For the latter transform, the sensitivity exhibits clear spatial structure, which is only slightly revealing itself in a CoV map.

deep neurons are provided. Surprisingly, sometimes sensitivity does not decrease (and even increases) with depth.

All networks show low sensitivity to permutation in terms of the first-order Sobol indices and Shapley values, indicating that constructed analysis mainly handles the augmentations themselves. As corresponding total Sobol indices are still high, we may conclude that permutation subtly affects the result through the interactions with other variables (as indirectly confirmed by the second-order Sobol indices rendered in the source-code repository). The same interpretation may be applied to the partition variable, sensitivity to which is captured by Shapley values (but neither first-order nor second-order Sobol indices): selection of training-validation partition is essential to networks but in a higher-level sense.

All sensitivity values reflect sensitivity to the class variable. Its first-order Sobol indices are increasing while moving to deeper layers, reflecting that almost all network components are involved in classifying, becoming more specialized to target recognition with depth.

Standalone constant sharpness and horizontal flip augmentations weakly influence the prediction (Table 1) but demonstrate different sensitivity patterns during simultaneous augmenting setup: there is a low sensitivity for sharpness adjustment (Shapley values, first-order Sobol indices) at convolutional checkpoints. In contrast, the horizontal flip has structured sensitivity patterns (Shapley values).

Rolling generates either border bar patterns (first-order Sobol) or more uniform global sensitivity involving interactions (Shapley values). Local patterns appear for erasing and elliptic local blur augmentations (first-order Sobol, Shapley). Erasing affects both the predictions and activations severely, i.e., networks more easily compensate for the elliptic blurring as more local transform which preserves more information.

All networks demonstrated strong sensitivity to grayscaling. This sensitivity expectedly intersects with one to saturation for specific units since grayscale is a limit-case of this transform. A hue transform is another colour adjustment that strongly impacts both sensitivity and accuracy, indicating the importance of a natural colour palette.

3.1.3. Correlation patterns

Correlation matrices between SA variables are plotted in Figures S7.2.1 (a)–(e), S7.2.2 (a)–(c). Correlations within the augmentation set tend towards a common level as checkpoints progress deeper, clustering variables together and smoothing their impact. Grayscale and saturation/hue have a strong correlation by means of the first-order Sobol indices and Shapley values. For the beginning checkpoints, it tends to correlate more with saturation, giving way to a correlation with hue in the deeper layers. In both cases, these correlations decay to zero as checkpoints move closer to the avgpool (however, Alexnet breaks the pattern exactly at this checkpoint). Hue and saturation variables are also correlated, and their correlation decays to zero or their cluster’s common level. Other notable positive correlations are observed for pairs from {hflip, rolling, rotation}, in terms of Shapley values. Total Sobol indices distinguish the erasing transform as significantly spaced away from other augmentations, forming the distinct cluster for several checkpoints closer to the beginning of a network. A similar trend to constitute a separate cluster is slightly less pronounced for a hue variable and even less prominent for grayscale and saturation.

3.1.4. Spatial correlation maps

Spatial correlation maps relating the SA variables and CoVs can be found in Supplementary materials as Figures S7.3.1 (a)–(c), S7.3.2 (a)–(b). The class variable has near-zero correlations for total Sobol indices measured at the final (classifying) checkpoint. In addition, for single augmentations the final-layer sensitivity shares either the inhibition pattern or near-zero correlations, suggesting that the activations loose augmentation-explained variability there. Correlation patterns based on Shapley values for the last layer are more diverse than ones for Sobol indices, and the common trend for all considered networks is the same near-zero or weak positive correlation for the class variable and weak negative correlation for the partition variable. For convolutional checkpoints, there are complete correlation maps, which may be viewed as spatial on-off patterns similar to ones in biological networks: positive correlation areas reflect the level of aligned matching between sensitivity and activation corresponding to excitation patterns, and negative correlations can be related to inhibition patterns. And similarly to biological networks [55, 56], the corresponding receptive fields demonstrate both center-surrounding and distributed structures. These spatial patterns depend on network, dataset, checkpoint, and SA variable, as well as on sensitivity values. Distributed patterns are minor for total Sobol indices, while the first-order Sobol indices and Shapley values exhibit both. As in biological neurons, the on-off fluctuations exist [57]: for a fixed network, the class or partition spatial correlation maps are similar in general but locally different depending on the augmentation set.

3.1.5. Linear discriminant analysis

Confusion matrices derived from cross-validated LDA are presented in Figures S7.4.1 (a)–(c), S7.4.2 (a)–(b). These results are detailed in [Appendix B](#); here, we summarize the common tendencies. SA variables are well separated at the first checkpoint for all values and networks except AlexNet trained on the Places 365 dataset (see remark in [3.1.1](#)). This separability decays while moving deeper, which is agreed with previously identified correlational patterns. Strong separation of erasing transform lasts longer again, even in the deepest checkpoints. The possible explanation for this pattern is that it causes severe distortions which are difficult to compensate for and easy to detect even with a linear classifier. Also, the closer to the classifying layer a checkpoint is located, the more separable the class variable becomes - there are either U-shaped or nearly parallel trends, along with poorer separability of certain augmentation variables. That may stem from the cancellation of augmentation impact and retargeting of neurons to the class variable as a network complying with the inference’s goal and learning higher-level abstractions.

3.2. Pattern analysis for damaged activations

The following results were obtained by applying guided masking on activations from convolutional checkpoints during inference.



Figure 4: Correlation patterns extracted by guided damaging of activations during inference. The darker colours correspond to the lower values of correlation. Each item within a single heatmap is a Spearman correlation between augmented and non-augmented masked inputs. Rows correspond to augmentations used for transforming the input, and columns give the SA variables as sources for building masks. Sensitivity values are designated as follows: *shpv* are Shapley values, and *si* and *sit* are the first-order and total Sobol indices, respectively.

3.2.1. Correlation patterns

Figure 4 presents the matching results for input augmentations and guided activation masking. Certain pairs for Shapley values and first-order Sobol indices are the most selective: Gaussian blur, grayscale, erasing, and hue transforms are the most diverging when masking and augmentation variables coincide, resulting in lower diagonal values. It supports the matching between computed sensitivity values and real network sensitivity. Total Sobol indices break this pattern in most cases (except grayscale and a few other partial entries), presumably due to their structure incorporating higher-level interactions among SA variables.

On the first augmentation set, the erasing transform separates well for Shapley values and for Sobol indices (exceptions: AlexNet, erasing-permutation pair dominates erasing-erasing on the ImageNet dataset; ResNet18 - all values are high, but still separable on the Places 365); for total Sobol indices, entries deviate significantly on all pairs. The grayscaling is separable in the case of AlexNet and VGG11 for all sensitivity values; ResNet18's entries are either close to one (ImageNet, Shapley) or diverging. The Gaussian blur's matching is rarely impaired (VGG11, Shapley values; all networks, total Sobol indices). The rolling is well-discriminated for Sobol indices (except for ResNet18, Places 365) and for AlexNet's Shapley values (ImageNet).

On the second augmentation set, AlexNet’s and VGG11’s results are aligned on the ImageNet dataset: both networks showed selective sensitivity to elliptical local blurring and rotation for Sobol indices. The horizontal flipping resulted in a correlation coefficient of nearly one for all sensitivity values, networks, and datasets. The rest, colour adjustments, are highly cohesive. The brightness is separable in many cases (even

for total Sobol indices, VGG11 and ResNet18, ImageNet), but susceptible to confounding with other SA variables in the case of ResNet18 (Shapley values, the first-order Sobol indices). The hue adjustment is well-paired with the same SA variable masking, although partially overlapped with the saturation variable. The saturation itself is mostly entangled with hue and slightly with contrast (ResNet18, ImageNet; AlexNet, Places 365). The contrast transformation matches well with its masking for all ResNet18’s sensitivity values (with the only exception, Sobol indices on the Places 365), though it is highly affected by other SA variables (especially other colour adjustments) and tangled with saturation for AlexNet’s and VGG11’s Shapley values.

In addition, for erasing, hue, contrast, Gaussian blur, and grayscale augmentations, masking with the other variables significantly affects predictions, indicating the possible instabilities related to these augmentations. This view is supported by the baseline measurements given in Table 1, as well as the patterns described in the previous subsection. It may also indicate the intersections among sensitivity maps, and the more local it is, the weaker the prediction pattern affected (for instance, horizontal flipping, local elliptic blur; erasing is not so localized, especially in deeper checkpoints). Although sharpness adjustment by a constant factor has little effect on regular predictions, it is a global augmentation; hence, other variables influence its prediction pattern. Interestingly, on ImageNet, it is affected mainly by a Gaussian blur variable, which operates with the same abstract property (sharpness). As for Places 365, this pattern is reversed (ResNet18), and the blurred input tends to be affected by the sharpness variable.

For additional findings extracted with hierarchical clustering analysis (HCA), we refer the reader to [Appendix C](#).

3.2.2. Single-class sensitivity to augmentations

Tables 2–4 list the top-5 classes sensitive to considered augmentations according to conducted sensitivity analysis. Corresponding selectivity patterns are problematic to be deduced by divergent values only. Thus, we matched sensitive classes and top-5 masked predictions by means of the Jaccard index (Tables S7.6.1 (a)–(f), S7.6.2 (a)–(f)) and highlighted the outliers according to the precomputed threshold values (see [Appendix D](#)). Table 5 is provided separately since it contains the most prominent evidence of proper sensitive class selection manifested as a substantial increase of Jaccard indices for erasing augmentation applied to AlexNet’s input. The objects of corresponding classes (*screen*; *monitor*; *television*; see Table 3) contain a filled rectangular pattern, similar to the results of applying the erasing transform. Other notable examples are classes containing light-shadow or edge contrast claimed as sensitive to contrast adjustment (*cliff dwelling*; *jigsaw puzzle*). Detailed analysis of other classes and their augmentation sensitivity is provided in [Appendix E](#).

3.3. Cutting off submodules of a network

Corresponding unitwise-averaged correlation matrices are presented in Figures S7.7 (a)–(d) (ImageNet only). They were further processed to extract higher-level correlation patterns (Figure 5) between single-channel segments (a) and channel-original matches (b). As for AlexNet, the value and saturation components are the most and least correlated to the original, respectively. Its successive checkpoints also tend to be more correlated, which could be due to their coherence emerged through training. ResNet18 shares the same channel ordering but exhibits a stronger correlation level irrespective of checkpoint distances, which can be explained by skip-connections leading to longer distortion retention. The most diverging correlations are observed for checkpoints close to the input (both networks) and fully connected layers (AlexNet). The first pattern can reflect the misalignment in data passed and input layers tuned to specific channels and value ranges. The second case might have arisen due to the suppression of spatial details by adaptive average pooling: this layer decreases the spatial dimensionality and minimizes the overlapping regions, resulting in specific data smoothing, which merges local patterns.

For channel-original matching, there is no diagonal dominance and, respectively, no exclusive similarity between isolated and non-isolated segments of the same checkpoints. They match together in different positions despite the input data differences, which could mean that relative sensitivity to augmentations translates through the whole convolutional part of a network to a reasonable extent. There is a decrease in some correlations for distant original checkpoints, which can be explained by gradual discrepancy accumulation.

Table 2: The most sensitive classes, according to the sensitivity analysis (Shapley values) performed on the last (classifying) layer (ILSVRC). Items are listed in the following format: class name (class index / sensitivity value).

	AlexNet	VGG11	ResNet18
Erasing (A _{1.1})	rock python (62/.58) magnetic compass (635/.54) paperknife (623/.54) maraca (641/.52) ladle (618/.51)	Hungarian pointer (211/.89) centipede (79/.88) poke bonnet (452/.84) thatched roof (853/.69) Doberman (236/.68)	beaker (438/.49) hussar monkey (371/.46) swimming cap (433/.45) ski mask (796/.44) drilling platform (540/.44)
Sharp. (A _{1.2})	church (497/.29) banister (421/.28) bee eater (92/.28) leaf beetle (304/.28) overskirt (689/.27)	ram, tup (348/.48) Pomeranian (259/.41) vestment (887/.38) kimono (614/.38) triumphal arch (873/.36)	poncho (735/.32) harvester, reaper (595/.28) Windsor tie (906/.27) face powder (551/.26) grasshopper (311/.25)
Rolling (A _{1.3})	mashed potato (935/.50) platypus (103/.48) cardigan (474/.47) cradle (516/.45) head cabbage (936/.42)	Scotch terrier (199/.67) Australian terrier (193/.66) harmonica (593/.65) chain saw (491/.61) barracouta (389/.59)	chocolate sauce (960/.50) English spaniel (217/.40) neck brace (678/.38) rock crab (119/.38) trilobite (69/.37)
Grayscale (A _{1.4})	Brittany spaniel (215/.34) tennis ball (852/.34) police van (734/.34) sea slug (115/.33) Welsh spaniel (218/.33)	Holocanthus tricolor (392/.56) American lobster (122/.53) briard (226/.52) African crocodile (49/.46) salamandra (25/.46)	coral reef (973/.39) wig (903/.32) Irish setter (213/.32) lakeside (975/.30) napkin (529/.30)
Gaus.blur (A _{1.5})	mask (643/.50) dingo (273/.46) European gallinule (136/.42) coho salmon (391/.40) soup bowl (809/.38)	pencil box (709/.61) eel (390/.57) harvester (595/.52) stole (824/.52) panda (388/.51)	affenpinscher (252/.44) vestment (887/.44) broom (462/.43) green snake (55/.38) hair slide (584/.36)
Bright. (A _{2.1})	hatchet (596/.37) Indian cobra (63/.35) miniskirt (655/.35) Gordon setter (214/.35) plate rack (729/.33)	howler monkey, howler (379/.53) plate (923/.49) worm fence (912/.49) boxer (242/.46) china cabinet (495/.44)	bookshop (454/.49) stove (827/.40) cliff, drop (972/.36) scabbard (777/.32) king snake (56/.31)
Contrast. (A _{2.2})	napkin (529/.45) pig (341/.39) basenji (253/.37) malinois (225/.34)	vestment (887/.51) parking meter (704/.49) jigsaw puzzle (611/.48) gyromitra (993/.48) waffle iron (891/.46)	Irish terrier (184/.41) Australian terrier (193/.36) drumstick (542/.35) wing (908/.34)
Satur. (A _{2.3})	African crocodile (49/.33) holster (597/.40) refrigerator (760/.37) boa constrictor (61/.35) whiptail lizard (41/.33)	screen (782/.65) wombat (106/.59) rifle (764/.49) water bottle (898/.46) three-toed sloth (364/.44)	holster (597/.34) nipple (680/.38) dough (961/.38) sandbar (977/.37)
Hue (A _{2.4})	rotisserie (766/.31) bluetick (164/.41) spaghetti squash (940/.39) hen-of-the-woods (996/.38) bloodhound (163/.37)	wok (909/.54) Lakeland terrier (189/.46) fox squirrel (335/.46) jeep (609/.45) orangutan (365/.44)	walking stick (313/.36) electric switch (844/.34) chiffonier (493/.62) pizza (963/.38)
Hflip (A _{2.5})	boxer (242/.37) conch (112/.32) plunger (731/.26)	lab coat (617/.39) cheetah (293/.38) bull mastiff (243/.37) drum (541/.35)	radiator (753/.36) wheaten terrier (202/.35)
Rotation (A _{2.6})	hatchet (596/.26) oxcart (690/.25) limousine (627/.24)	cocktail shaker (503/.32) platypus (103/.59) buckle (464/.54)	paddle wheel (694/.35) carbonara (959/.25) blowfish (397/.23)
El.loc.blur (A _{2.7})	solar collector (807/.48) basset hound (161/.37) punch bag (747/.36) sliding door (799/.36) breakwater (460/.36)	face powder (551/.51) paddlewheel (694/.50) bathtub (435/.49)	groom (982/.22) horizontal bar (602/.22) Norfolk terrier (185/.22)
	hippopotamus (344/.52) albatross (146/.48) Sussex spaniel (220/.48) water snake (58/.46) paperknife (623/.46)	scabbard (777/.76) dishwasher (534/.65) computer mouse (673/.65) wreck (913/.58) mosque (668/.57)	hotpot (926/.36) shoji (789/.33) hyena (276/.31) weasel (356/.30)

Table 3: The most sensitive classes, according to the sensitivity analysis (the first-order Sobol indices) performed on the last (classifying) layer (ILSVRC). Items are listed in the following format: class name (class index / sensitivity value).

	AlexNet	VGG11	ResNet18
Erasing (A _{1.1})	screen (782/.06) television (851/.05) monitor (664/.04) lighter (626/.03) pedestal (708/.03)	warthog (343/.17) tree frog (31/.10) scuba diver (983/.07) safe (771/.05) fiddler crab (120/.03)	wardrobe (894/.04) frilled lizard (43/.03) television (851/.02) monitor (664/.02) screen (782/.02)
Sharp. (A _{1.2})	affenpinscher (252/.03) rubber (767/.02) drumstick (542/.01) steel drum (822/.01) Great Dane (246/.01)	warthog (343/.11) coho salmon (391/.10) ladle (618/.03) Alaskan malamute (249/.02) carton (478/.02)	wardrobe (894/.05) overskirt (689/.02) lighthouse (437/.02) jackfruit (955/.02) gazelle hound (176/.01)
Rolling (A _{1.3})	Appenzeller (240/.02) vault (884/.01) cabbage butterfly (324/.01) grand piano (579/.01) drilling platform (540/.01)	black grouse (80/.04) space shuttle (812/.04) ricksha (612/.03) grocery store (582/.03) cliff dwelling (500/.02)	English spaniel (217/.03) flat-coated retriever (205/.02) toilet seat (861/.01) strawberry (949/.01)
Grayscale (A _{1.4})	tree frog (31/.04) affenpinscher (252/.03) Shetland sheepdog (230/.03) missile (657/.03) television (851/.03)	warthog (343/.16) tree frog (31/.10) scuba diver (983/.07) space shuttle (812/.05) Russian wolfhound (169/.04)	German short-haired pointer (210/.01) tree frog (31/.02) sweatshirt (841/.02) lifeboat (625/.02) chain (488/.02)
Gaus.blur (A _{1.5})	wastebin (412/.03) affenpinscher (252/.03) tub, vat (876/.03) bucket (463/.02) beaker (438/.02)	flat-coated retriever (205/.08) scuba diver (983/.07) stove (827/.06) bubble (971/.06) coho salmon (391/.06)	Shetland sheepdog (230/.02) three-toed sloth (364/.03) English spaniel (217/.03) hare (331/.02) sleeping bag (797/.02)
Bright. (A _{2.1})	Weimaraner (178/.04) mailbox (637/.04) koala (105/.03) frilled lizard (43/.02) pipe organ (687/.02)	Bedlington terrier (181/.08) pinwheel (723/.03) Weimaraner (178/.03) grey wolf (269/.03) barrel, cask (427/.03)	upright piano (881/.02) ambulance (407/.02) cellular phone (487/.01) Psittacus erithacus (87/.01) hippopotamus (344/.01)
Contrast. (A _{2.2})	walking stick (313/.03) red-breasted merganser (98/.03) pay-phone (707/.02) chain (488/.02)	cliff dwelling (500/.12) jigsaw puzzle (611/.11) cornet (513/.06) shovel (792/.05)	jigsaw puzzle (611/.05) convertible (511/.03) bubble (971/.02) spotlight, spot (818/.01)
Satur. (A _{2.3})	sock (806/.02) hay (958/.06) cliff dwelling (500/.03) indris (384/.02)	snow leopard (289/.04) cliff dwelling (500/.21) wardrobe (894/.08) sea urchin (328/.04)	hook, claw (600/.01) jellyfish (107/.02) gown (578/.02) bubble (971/.02)
Hue (A _{2.4})	moped (665/.02) sea urchin (328/.02) Weimaraner (178/.04) agaric (992/.03)	barbell (422/.04) grey wolf (269/.04) cliff dwelling (500/.20) house finch (12/.18)	upright piano (881/.02) sturgeon (394/.01) bee (309/.03) cabbage butterfly (324/.02)
Hflip (A _{2.5})	missile (657/.03) Chihuahua (151/.03) vine snake (59/.02) giant schnauzer (197/.02)	salamandra (25/.07) breastplate (461/.06) missile (657/.04) cliff dwelling (500/.16)	china cabinet (495/.02) digital clock (530/.02) jellyfish (107/.01) Granny Smith (948/.03)
Rotation (A _{2.6})	missile (657/.02) shield (787/.02) moped (665/.02) snowmobile (802/.02)	shield (787/.07) Siberian husky (250/.04) snowmobile (802/.03) missile (657/.03)	nipple (680/.02) fur coat (568/.02) combination lock (507/.02) sturgeon (394/.01)
El.loc.blur (A _{2.7})	jeep (609/.03) napkin (529/.03) red-breasted merganser (98/.03) Dandie Dinmont terrier (194/.02)	husky (248/.07) ruffed grouse (82/.06) bullfrog (30/.06) beaker (438/.04)	tray (868/.04) cellular phone (487/.03) military uniform (652/.03) mushroom (947/.02)
	leafhopper (317/.02) sport car (817/.02) golf cart (575/.02) bulletproof vest (465/.02)	Siberian husky (250/.04) cliff dwelling (500/.20) barrel, cask (427/.07) parking meter (704/.07)	coyote (272/.01) apron (411/.03) cleaver (499/.02) lacewing fly (318/.01)
	black and gold garden spider (72/.02) cup (968/.01)	coyote (272/.03) cornet (513/.03)	stingray (6/.01) odometer (685/.01)

Table 4: The most sensitive classes, according to the sensitivity analysis (Shapley values and the first-order Sobol indices) performed on the last (classifying) layer (Places 365). Items are listed in the following format: class name (class index / sensitivity value).

		Shapley values		Sobol indices	
		AlexNet	ResNet18	AlexNet	ResNet18
Erasing (A1.1)	orchard (249/.53)	ice cream parlor (185/.36)	home theater (177/.07)	home theater (177/.08)	television room (328/.05)
	temple asia (330/.36)	lagoon (204/.34)	movie theater indoor (235/.04)	movie theater indoor (235/.03)	server room (298/.02)
	village (348/.33)	archaeological excavation (13/.30)	television room (328/.04)	barndoar (41/.02)	harbor (171/.02)
	greenhouse indoor (165/.33)	gymnasium indoor (168/.29)	phone booth (263/.03)	church outdoor (91/.01)	gazebo exterior (159/.01)
	beer garden (53/.31)	corral (105/.29)	barndoar (41/.03)	elevator lobby (130/.01)	temple asia (330/.01)
	delicatessen (114/.18)	delicatessen (114/.14)	motel (231/.02)	church outdoor (91/.02)	church outdoor (91/.02)
	bazaar outdoor (47/.16)	veterinarians office (346/.14)	field wild (141/.01)	ballroom (35/.01)	ballroom (35/.01)
Sharp. (A1.2)	excavation (136/.15)	garage indoor (156/.13)	building facade (67/.01)	rope bridge (291/.01)	rope bridge (291/.01)
	art school (20/.14)	islet (194/.13)	ball pit (34/.01)	pond (271/.01)	pond (271/.01)
	lawn (209/.14)	tundra (341/.13)	canal urban (79/.01)	aquarium (9/.01)	aquarium (9/.01)
	field road (142/.42)	underwater ocean deep (342/.29)	throne room (331/.02)	park (254/.02)	park (254/.02)
	canyon (81/.38)	hotel outdoor (181/.28)	galley (155/.01)	church outdoor (91/.02)	church outdoor (91/.02)
	rice paddy (287/.36)	tree house (339/.25)	nursery (240/.01)	swimming pool outdoor (326/.02)	swimming pool outdoor (326/.02)
	dining room (121/.26)	greenhouse outdoor (166/.24)	bar (39/.01)	pet shop (261/.01)	pet shop (261/.01)
Rolling (A1.3)	wave (357/.25)	natural history museum (239/.24)	movie theater indoor (235/.01)	playroom (269/.01)	playroom (269/.01)
	mountain path (233/.33)	topiary garden (333/.25)	hospital room (179/.04)	coffee shop (99/.02)	coffee shop (99/.02)
	lawn (209/.30)	general store indoor (160/.23)	archive (14/.03)	barndoar (41/.02)	barndoar (41/.02)
	sandbox (294/.26)	swimming pool outdoor (326/.23)	music studio (238/.03)	server room (298/.01)	server room (298/.01)
	flea market indoor (146/.25)	crevasse (111/.22)	coffee shop (99/.03)	shed (299/.01)	shed (299/.01)
	florist shop indoor (147/.25)	florist shop indoor (147/.21)	physics laboratory (264/.03)	ballroom (35/.01)	ballroom (35/.01)
	market indoor (222/.31)	courtyard (109/.29)	throne room (331/.02)	rock arch (289/.02)	rock arch (289/.02)
Grayscale (A1.4)	childs room (89/.24)	playroom (269/.26)	shed (299/.02)	bazaar indoor (46/.02)	bazaar indoor (46/.02)
	shoe shop (300/.23)	basement (43/.25)	barndoar (41/.02)	berth (55/.02)	berth (55/.02)
	driveway (127/.23)	fabric store (137/.22)	temple asia (330/.02)	playroom (269/.02)	playroom (269/.02)
	kitchen (203/.22)	patio (259/.22)	restaurant (284/.02)	waiting room (352/.02)	waiting room (352/.02)
	pizzeria (267/.30)	dressing room (126/.26)	childs room (89/.03)	desert vegetation (117/.02)	desert vegetation (117/.02)
	patio (259/.22)	corral (105/.21)	playroom (269/.03)	television studio (329/.02)	television studio (329/.02)
	general store outdoor (161/.21)	pier (266/.20)	creek (110/.02)	music studio (238/.02)	kindergarten classroom (202/.01)
Bright. (A2.1)	crosswalk (112/.21)	locker room (219/.20)	candy store (80/.02)	art studio (21/.02)	pasture (258/.01)
	childs room (89/.19)	loading dock (216/.20)	archaeological excavation (13/.28)	television studio (329/.02)	pet shop (261/.01)
	village (348/.26)	archaeological excavation (13/.28)	army base (18/.28)	music studio (238/.02)	ice shelf (187/.04)
	balcony exterior (32/.24)	utility room (343/.24)	utility room (343/.24)	childs room (89/.02)	discotheque (122/.03)
	promenade (273/.23)	veterinarians office (346/.23)	veterinarians office (346/.23)	amusement arcade (6/.01)	stage indoor (315/.03)
	biology laboratory (56/.20)	volleyball court outdoor (351/.23)	volleyball court outdoor (351/.23)	stage indoor (315/.01)	stage indoor (315/.03)
	creek (110/.20)	garage outdoor (157/.28)	garage outdoor (157/.28)	discotheque (122/.06)	candy store (80/.03)
Contrast. (A2.2)	archaeological excavation (13/.26)	kindergarten classroom (202/.23)	kindergarten classroom (202/.23)	ice shelf (187/.04)	ice floe (186/.03)
	balcony interior (33/.25)	beer hall (54/.22)	beer hall (54/.22)	stage indoor (315/.04)	ice floe (186/.03)
	restaurant kitchen (285/.23)	bookstore (60/.22)	bookstore (60/.22)	ball pit (34/.04)	vegetable garden (345/.03)
	trench (340/.23)	sauna (295/.20)	sauna (295/.20)	ice floe (186/.03)	florist shop indoor (147/.03)
	wet bar (358/.21)	kasbah (200/.37)	kasbah (200/.37)	botanical garden (62/.03)	beer hall (54/.02)
	recreation room (281/.25)	landfill (206/.30)	landfill (206/.30)	vegetable garden (345/.03)	discotheque (122/.02)
	slum (308/.24)	rainforest (279/.27)	rainforest (279/.27)	stage indoor (315/.03)	botanical garden (62/.02)
Satur. (A2.3)	ruin (292/.24)	fishpond (145/.26)	fishpond (145/.26)	florist shop indoor (147/.03)	japanese garden (197/.01)
	beer hall (54/.24)	fastfood restaurant (139/.25)	fastfood restaurant (139/.25)	rainforest (279/.02)	hospital room (179/.01)
	plaza (270/.23)	residential neighborhood (283/.17)	residential neighborhood (283/.17)	basement (43/.01)	cottage (107/.01)
	sandbox (294/.15)	zen garden (364/.14)	zen garden (364/.14)	forest road (152/.01)	market outdoor (223/.01)
	general store indoor (160/.14)	catacomb (85/.13)	catacomb (85/.13)	candy store (80/.01)	aqueduct (10/.01)
	fishpond (145/.13)	diner outdoor (119/.11)	diner outdoor (119/.11)	church indoor (90/.01)	office (244/.01)
	trench (340/.12)	food court (148/.11)	food court (148/.11)	staircase (317/.01)	cottage (107/.01)
Hue (A2.4)	locker room (219/.12)	office (244/.22)	office (244/.22)	street (319/.02)	vegetable garden (345/.01)
	driveway (127/.28)	village (348/.22)	village (348/.22)	golf course (164/.01)	football field (149/.01)
	boat deck (58/.27)	oast house (242/.20)	oast house (242/.20)	ticket booth (332/.01)	florist shop indoor (147/.01)
	campus (77/.26)	ski slope (305/.20)	ski slope (305/.20)	atrium public (25/.01)	lecture room (210/.02)
	clothing store (96/.23)	home office (176/.19)	home office (176/.19)	field cultivated (140/.01)	youth hostel (363/.02)
	bakery shop (31/.23)	hangar outdoor (170/.33)	hangar outdoor (170/.33)	beer hall (54/.03)	hospital room (179/.02)
	galley (155/.43)	desert sand (116/.33)	desert sand (116/.33)	forest road (152/.01)	dining hall (120/.01)
El.loc.blur (A2.7)	nursing home (241/.37)	desert vegetation (117/.31)	desert vegetation (117/.31)	rice paddy (287/.01)	greenhouse indoor (165/.01)
	entrance hall (134/.32)	elevator lobby (130/.31)	elevator lobby (130/.31)	stage outdoor (316/.01)	
	kitchen (203/.29)	residential neighborhood (283/.28)	residential neighborhood (283/.28)	rope bridge (291/.01)	
	general store indoor (160/.29)				

Table 5: Mean Jaccard indices between top-5 masked predictions and top-5 sensitive classes extracted by using Sobol indices computed for the final (classifying) layer. The sensitivity analysis variable used for masking (convolutional checkpoints only) is the same as the input augmentation. Activations corresponding to the $(1 - q) \cdot 100\%$ top sensitivity values per checkpoint were multiplied by $\alpha = 1.5$ during inference. Values higher than the interquartile-based threshold τ are underlined.

Imagenet (ILSVRC)															
Augmentation of input	AlexNet				VGG11				ResNet18						
	q=0.5	q=0.6	q=0.7	q=0.8	q=0.9	q=0.5	q=0.6	q=0.7	q=0.8	q=0.9	q=0.5	q=0.6	q=0.7	q=0.8	q=0.9
Erasing	.0672	.0791	.0883	.1007	.1373	.0018	.0012	.0007	.0005	.0009	.0024	.0031	.005	.0055	.0053
Sharp.	.0024	.0028	.0028	.0028	.0028	<u>.0048</u>	<u>.0043</u>	<u>.0042</u>	<u>.0041</u>	<u>.0039</u>	.0003	.0005	.0008	.0013	.0018
Rolling	.0025	.0024	.002	.0017	.0016	.0023	.0026	.0026	.0027	.0029	.0003	.0005	.0009	.0011	.0018
Grayscale	<u>.0033</u>	<u>.0034</u>	<u>.0034</u>	.003	.003	<u>.0033</u>	<u>.0032</u>	<u>.0033</u>	<u>.0031</u>	<u>.0028</u>	<u>.0139</u>	<u>.0155</u>	<u>.0092</u>	<u>.0044</u>	<u>.0033</u>
Gaus.blur	.0017	.002	.0021	.0021	.0024	.0022	.0024	.0029	<u>.0031</u>	.0027	.0001	.0002	.0003	.0012	.0017
Bright.	.0017	.0016	.0017	.0016	.0015	.0021	.002	.0019	.0017	.0017	.0002	.0002	.0005	.0008	.0013
Contrast.	<u>.0034</u>	<u>.0036</u>	<u>.0037</u>	<u>.0038</u>	<u>.0041</u>	<u>.0033</u>	<u>.0035</u>	<u>.0035</u>	<u>.0036</u>	<u>.0037</u>	<u>.0812</u>	<u>.0834</u>	<u>.0872</u>	<u>.0888</u>	<u>.0661</u>
Satur.	<u>.0095</u>	<u>.0072</u>	<u>.0054</u>	<u>.0041</u>	<u>.0034</u>	<u>.0126</u>	<u>.0098</u>	<u>.0075</u>	<u>.0056</u>	<u>.0049</u>	<u>.0058</u>	<u>.0127</u>	<u>.0188</u>	<u>.0177</u>	<u>.0176</u>
Hue	.0028	.0027	.0028	<u>.0032</u>	<u>.0045</u>	.0009	.0009	.0008	.0008	.001	<u>.0468</u>	<u>.0397</u>	<u>.0305</u>	<u>.031</u>	<u>.0325</u>
Hflip	.0024	.0029	.003	<u>.0033</u>	<u>.0034</u>	.0018	.0023	.0024	.0027	.0028	.0001	.0021	.0021	.0024	.0028
Rotation	.002	.0021	.0022	.0023	.0025	.0027	.0029	.003	<u>.0031</u>	<u>.0031</u>	.0015	.0024	<u>.0033</u>	<u>.004</u>	<u>.0042</u>
El.loc.blur	.0027	.0028	<u>.0031</u>	<u>.0033</u>	<u>.0033</u>	.0019	.002	.0021	.0022	.0023	<u>.0031</u>	<u>.004</u>	<u>.0041</u>	<u>.0046</u>	<u>.0043</u>

Places 365																
Augmentation of input	AlexNet				ResNet18											
	q=0.5	q=0.6	q=0.7	q=0.8	q=0.9	q=0.5	q=0.6	q=0.7	q=0.8	q=0.9						
Erasing	<u>.0888</u>	<u>.1101</u>	<u>.1412</u>	<u>.2</u>	<u>.2434</u>	<u>.0249</u>	<u>.0316</u>	<u>.0334</u>	<u>.0434</u>	<u>.0672</u>						
Sharp.	.005	.0052	.0054	.0056	.0056	<u>.0096</u>	<u>.0093</u>	<u>.0095</u>	<u>.0092</u>	<u>.0089</u>						
Rolling	.0075	.0079	<u>.0083</u>	.008	.0067	.0065	<u>.0091</u>	<u>.0081</u>	.0054	.0042						
Grayscale	<u>.0232</u>	<u>.022</u>	<u>.0209</u>	<u>.0202</u>	<u>.0191</u>	.003	.0028	.0032	.0042	.0041						
Gaus.blur	.0076	.008	<u>.0088</u>	<u>.0096</u>	<u>.0091</u>	<u>.0119</u>	<u>.0143</u>	<u>.0135</u>	<u>.0085</u>	<u>.0074</u>						
Bright.	<u>.0239</u>	<u>.0265</u>	<u>.0267</u>	<u>.0297</u>	<u>.0218</u>	.0004	.0004	.0007	.0012	.0034						
Contrast.	<u>.037</u>	<u>.0473</u>	<u>.0639</u>	<u>.0907</u>	<u>.0845</u>	.0006	.0007	.0008	.001	.0021						
Satur.	<u>.0246</u>	<u>.029</u>	<u>.0332</u>	<u>.0598</u>	<u>.0726</u>	<u>.0452</u>	<u>.0638</u>	<u>.0764</u>	<u>.0748</u>	<u>.0617</u>						
Hue	<u>.0287</u>	<u>.033</u>	<u>.0382</u>	<u>.0579</u>	<u>.0563</u>	<u>.057</u>	<u>.0749</u>	<u>.0829</u>	<u>.0785</u>	<u>.0652</u>						
Hflip	.0051	.0055	.0057	.0059	.0075	.0017	.0038	<u>.0085</u>	<u>.0089</u>	<u>.0091</u>						
Rotation	.0064	.0065	.0068	<u>.0085</u>	<u>.0092</u>	.0048	.0055	.0059	.0063	.0065						
El.loc.blur	.0051	.0055	.0056	.006	.0059	.0023	.0044	.0045	.0039	.004						

4. Discussion

This work aimed to design a framework for studying neural networks by exploring the sensitivity of their inner activations to simultaneously applied augmentations, enriched with auxiliary variables. Sobol indices and Shapley values were used as the main computational tool, which requires a proper sampling scheme for applying augmentations to be employed. Resulting sensitivity maps provide a visualization which captures the individual sensitivity of single units within the checkpoint. Interestingly, the sensitivity to quite simple augmentations is observed up to the deepest layers, which is consistent with the findings from work [20], demonstrating low-level concept identification by deep neurons. Although visual inspection can assist in suggesting the trends, any analysis should be performed with caution due to the approximate nature of the results. We have used complementary ways of analysis through cross-validated LDA, which treats sensitivity maps as features to predict the SA variable, and unit-wise Spearman correlation, which indicates monotonic relationships between variables. Both techniques allowed us to reveal the data patterns at the expense of analysis capability on an individual unit level and showed consistent results. To validate the sensitivity value computations, we performed the guided neural damaging of the corresponding checkpoints. Extracted correlational patterns of matches between the most sensitive classes and top-5 masked predictions demonstrated specificity for a series of augmentations and networks. Partially the patterns are repeated for

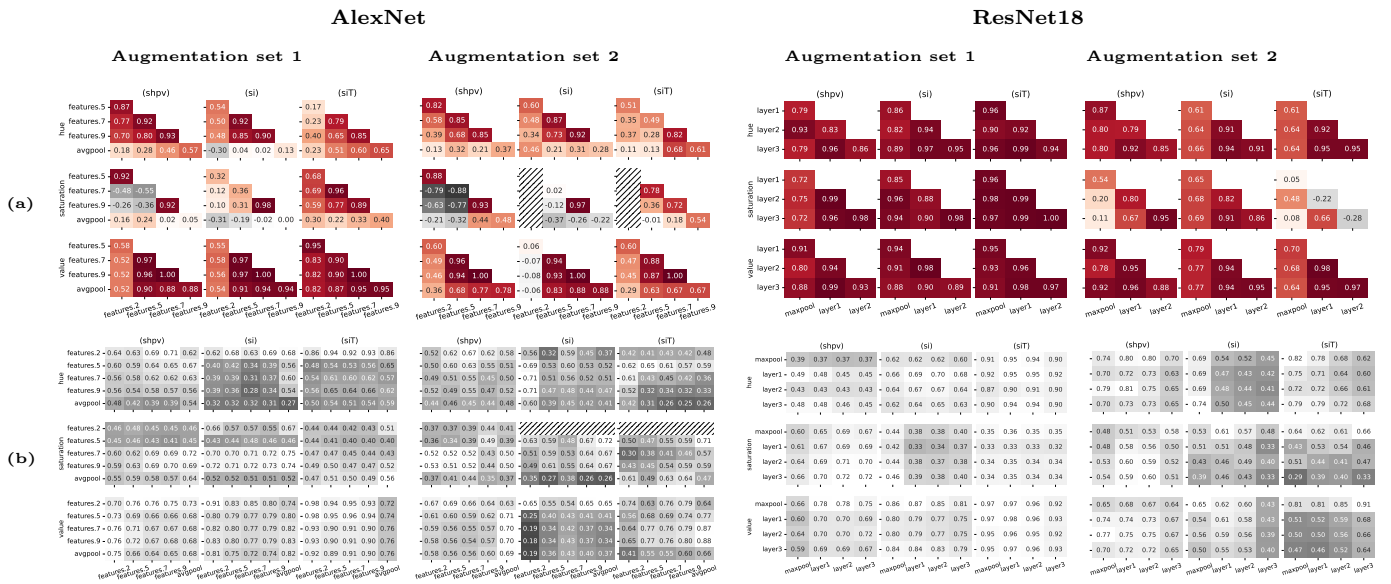


Figure 5: Higher-order correlation patterns extracted for the segments separated from their networks. At first, Spearman correlations between paired SA variables were computed at a checkpoint level for both isolated fixed-channel segments (H/S/V) and corresponding original parts. Then, the cross-correlations between triangular parts of these matrices were computed, matching different checkpoint levels. (a) Results for paired checkpoints within a fixed input channel (isolated segments only). Lighter colours encode correlations closer to zero (in their absolute value). (b) Matching the isolated and original segments. Darker colours correspond to lower values. Single heatmap legend: rows correspond to single-channel checkpoints, columns to ones of original. Both (a) and (b): hatched cells indicate constant input that could not be correlated.

fixed architecture on different datasets. Given that we omitted considering fine-tuned networks pretrained on other datasets (transfer learned models), it suggests that sensitivity may be also due to the intrinsic property of the architecture. The resembling patterns within similarly structured AlexNet and VGG11 (ILSVRC) also potentially indicate this.

For a long time the ImageNet was a leading dataset in deep learning, and it continues to be a pretraining basis for various computer vision models until now. In our research, bounded to the ILSVRC (as a subset of ImageNet on training partition and independently sampled on validation part), we thoroughly evaluated developed framework for three classic CNN architectures. The Table 1 implies that all of them still can be improved for a training part and experience an error rate gap between training and validation subsets, thus they are unlikely have surpassed the dataset limitations. Additionally we investigated sensitivity patterns of AlexNet and ResNet18 on the Places365 dataset, similarly to ILSVRC exhibiting the class and imaging conditions diversity, offering a sufficiently high resolution, and featuring accessible pretrained models (excluding VGG11).

Exploration of convolutional neural networks using the constructed framework has established that although a set of augmentations affects all their elements, different layers and neurons respond inhomogeneously to specific SA variables. Such preferences reflect the specialization of network elements that emerged during learning. The specialization changes with the depth of the networks: the closer to the output, the smaller the contribution of augmentations, and the higher the contribution of the class variable. In addition, activation maps reveal on-off patterns similar to those in biological neural networks, which also differ depending on the SA variable and the depth of the layer.

A specialization, thus, may be conceived as a sensitivity to changes in a certain property of input data manifested through the redistribution of the corresponding variable's contribution to a total variance. The framework proposed in this work is suitable for identifying the network components specialized in this sense. In general, such components are not isolated interfering with each other in terms of sensitivity, which was shown by the masked inference damaging. The top-1 accuracy-based approach used for building the feature space in this analysis provides an initial insight into tendencies, but it is a strong averaging that became

most apparent in the case of ResNet18 as the most resistant to distortions network under conditions of our study. To extract the correlation patterns for paired sources of distortions (augmentations and masks), it might be worth increasing the feature space dimensionality and using more specific scores like per-class accuracy, confusion matrices, their combinations with other metrics.

In addition, our findings support the idea of determining single-class sensitivity, which may be potentially utilized to suppress the impact of input distortions on classifying performance. Our approach is based on candidate filtering by co-occurrences of sensitive classes in predictions obtained through activation damaging. In general, this is not the only way to gather evidence supporting the correctness of a single-class sensitivity of the whole network by means of the sensitivity of the last classifying layer. Not less important is identifying the classes systematically inhibited by the network with edited activations. It is not obvious how to implement such a method, but it seems to be important as negative feedback and inhibition in biological neural networks.

Analysis of the network segments might be relevant for studying large models with expensive inference, and it is important to recognize the relationships between patterns in isolated and normal operating modes. Through matching the sensitivity measured in both operating modes, it was confirmed that sensitivity to augmentations depends on both input data and preceding transformations. A comparison of correlation patterns among the standalone units also uncovered that skip-connections may facilitate the continuation of the sensitivity patterns. That assumption is also supported by Table 1, according to which the ResNet18 have the smallest percentage decrease in accuracy while applying a single augmentation (the only exception is erasing for VGG11).

The method was supplied with a repeating of separate channels of HSV representation, and it may be modified by mapping the values to the expected interval of input values change. Other methods of studying the isolated segments may be proposed, e.g., to generate an activation maximization input and use it as a mask for the corresponding channel, or to generate multiple inputs of specific patterns, like fractal, geometric shapes, textures, noise distributions.

It is worth noting that the proposed sensitivity analysis framework utilizes the classification specifics only for single-class analysis. Auxiliary variables incorporate only the input's class and partition selection and the order of augmentations to be applied. In other words, they do not rely on the network structure, making it possible to reuse the framework for networks designed to solve other problems. Fundamental issue of the variance-based methods is a time-consuming necessity to make a sufficient number of samples. In our implementation, more robust scheme involves saving the sampled values on disc before computing sensitivity values, imposing additional requirements on the storage volume.

On the basis of sensitivity analysis, the methods of improving resistance to input distortions (including adversarial attacks) can be potentially developed in the form of guided activation corrections or fine-tuning. An important point is to analyze the total variances and coefficients of variation, high values of which may indicate instability. Another possible instability is connected with units that have low-valued coefficients of variation but can not be replaced by their means due to a strong response to small perturbations.

A number of parallels to the functioning of biological neurons were identified within the scope of this work. The latter are typically studied under a treatment-control paradigm involving a single modality [58]. At the same time, real biological systems solve multiple tasks simultaneously and operate in complex environments, enriched by multiple multi-modal inputs. Having adapted the sampling schemes and set the SA variables up, our framework seems to be promising to reveal the specifics of both artificial and biological neural networks under closer to real conditions.

Data availability

In our study, we employed the training and validation parts of the ImageNet large-scale visual recognition challenge (ILSVRC) dataset, which may be downloaded from the corresponding competition page at Kaggle: <https://www.kaggle.com/competitions/imagenet-object-localization-challenge>

ILSVRC uses the subset of Imagenet dataset as a training partition and provides its own validation (labelled) and test (no public labels) sets. Since the training part of the ILSVRC dataset is non-uniformly distributed among the classes and the minimal possible number of samples per class is 732, we used a subset

with $732 \cdot 1000$ samples to generate a training partition (controlled by a random seed). The validation partition has already been equalized by class (contains $50 \cdot 1000$ samples).

Another dataset used in our study is Places 365 [54], as it is derived from a large number (365 classes) of diverse images of relatively good resolution, and there are available CNN models trained from a scratch on this dataset. Similarly to the ILSVRC, its validation partition is already equalized (100 samples per class), and we balanced the number of samples of the training partition to be 3068 images per class.

<http://places2.csail.mit.edu>

Results of computational experiments regarding sensitivity values measured at checkpoints of the whole networks and corresponding segments and guided masked predictions are available at the corresponding Zenodo repositories:

<https://doi.org/10.5281/zenodo.18097911>

<https://doi.org/10.5281/zenodo.18098133>

Code availability

All models and computational experiments were implemented using the Python programming language under the conda package manager [59]. This study employed the following packages: pytorch [60], SALib [45], h5py [61], opencv [62], numpy [63], scipy [64], pandas [65, 66], scikit-learn [67], seaborn [68], matplotlib [69], and statsmodels [70]. The experiments were systematized using Jupyter Notebooks [71].

All source code, scripts, Jupyter notebooks produced within this study can be found at the GitHub repository:

https://github.com/kharyuk/activation_sa

Acknowledgements

Part of the work related to sensitivity analysis of the inner activations and its validation by guided masking prediction was supported by the Ministry of Science and Higher Education grant No. 075-15-2020-801. Single-class sensitivity analysis and sensitivity analysis of the network's segments were supported by Ministry of Science and Higher Education grant No. 075-10-2021-068.

CRediT author statement

P.K.: Conceptualization, Methodology, Software, Validation, Investigation, Data curation, Visualization, Writing - Original draft preparation, Reviewing and Editing; **S.M.:** Conceptualization, Resources, Writing - Reviewing and Editing; **I.O.:** Conceptualization, Resources, Funding acquisition.

S.M. and I.O. proposed the idea to analyze the sensitivity of neuronal activations using Sobol indices. P.K. suggested studying sensitivity to simultaneously applied augmentations, conducted research and developed the idea into the proposed framework. P.K. and S.M. contributed to the work on the text. I.O. provided administrative support.

Appendix A. Experimental setup details

In this section, we provide details of the inner augmentation parameters (Table A.1) as well as the setup for the first and the third experimental series (Tables A.2, A.3). As we mentioned in Subsection 2.2, inner variables were combined to extract the sensitivity values of separate augmentations.

The number of samples to compute the rank-biserial correlation coefficients is calculated as follows: $(1 + n_{\text{aug}} + m_{\text{inner}} \cdot n_{\text{aug},\theta}) \cdot k \cdot N_{\text{classes}}$, where $n_{\text{aug},\theta}$ and n_{aug} are the number of augmentations with and without inner parameters, m_{inner} - a number of samples for parameterized augmentations, N_{classes} - a number of classes in the dataset, k is a number of samples per class. In the case of the sampling scheme 1 (which uses Salteli sampler inside): $n_{\text{samples}} \cdot (2 \cdot d_i + 2)$, where n_{samples} is a number of samples (must be a power of 2), d_i - number of variables for the i -th augmentation set. The number of samples for computing Shapley

values is calculated in the following way: $n_{\text{perm.}} \cdot d_i \cdot n_{\text{outer}} \cdot n_{\text{inner}}$, where $n_{\text{perm.}}$ is a number of permutations, d_i is the similar number of variables for the i -th augmentation set, n_{outer} and n_{inner} are the numbers of outer and inner samples.

Table A.1: Inner parameters θ_i of augmentations considered in the study. Uniform_C(a, b) stands for continuous uniform distribution, Uniform_D(a, b) - discrete.

Augmentation	Random parameter	Distribution	Related parameters
(A _{1.1}) erasing	center _x center _y scale factor aspect ratio	Uniform _D ($w_{\text{offset}}, \text{width} - w_{\text{offset}}$) Uniform _D ($h_{\text{offset}}, \text{height} - h_{\text{offset}}$) Uniform _C (0.02, 0.33) LogUniform(0.3, 3.3)	$w_{\text{offset}} = \text{width}/5$ $h_{\text{offset}} = \text{height}/5$
(A _{1.2}) sharpness_const	–	–	sharpness factor = 1.5
(A _{1.3}) rolling	horizontal shift vertical shift	Uniform _D ($-w_{\text{offset}}, w_{\text{offset}}$) Uniform _D ($-h_{\text{offset}}, h_{\text{offset}}$)	$w_{\text{offset}} = \text{width}/5$ $h_{\text{offset}} = \text{height}/5$
(A _{1.4}) grayscale	–	–	–
(A _{1.5}) gaussian_blur	σ_{blur}	Uniform _C (0.1, 2)	kernel size = (7, 7)
(A _{2.1}) brightness	brightness factor	Uniform _C (0.1, 2.5)	–
(A _{2.2}) contrast	contrast factor	Uniform _C (0.01, 3.5)	–
(A _{2.3}) saturation	saturation factor	Uniform _C (0.01, 3.5)	–
(A _{2.4}) hue	hue factor	Uniform _C (-0.5, 0.5)	–
(A _{2.5}) horizontal flip	–	–	–
(A _{2.6}) rotation	angle (degree)	Uniform _C (-10, 10)	–
(A _{2.7}) elliptic_local_blur	angle (degree) semi-major axis semi-minor axis center shift _x center shift _y	Uniform _C (-15, 15) Uniform _D (10, 32) Uniform _D (10, 32) Uniform _D (-32, 32) Uniform _D (-32, 32)	$\sigma_{\text{blur}} = 2$

Table A.2: Details of the first experimental series: number of activations (summed over all checkpoints; global) and number of samples for each unit per experiment. Rank biserial correlation coefficient ($rbscc$); sampling scheme 1: means and variances ($sitv$), Sobol indices (si); sampling scheme 2: means and variances ($shptv$), Shapley values ($shpv$).

	AlexNet	VGG11	ResNet18
Num.activations	$ \begin{aligned} & 46656 + 32448 + 64896 \\ & + \underbrace{3264}_{\text{features.2}} + \underbrace{9216}_{\text{features.5}} + \underbrace{4096}_{\text{features.7}} \\ & + \underbrace{4096}_{\text{features.9}} + \underbrace{1000}_{\text{avgpool}} \\ & + \underbrace{4096}_{\text{classifier.5}} + \underbrace{1000}_{\text{classifier.6}} \\ = & 205672 \end{aligned} $	$ \begin{aligned} & 802816 + 401408 + 200704 \\ & + \underbrace{100352}_{\text{features.2}} + \underbrace{25088}_{\text{features.5}} + \underbrace{4096}_{\text{features.10}} \\ & + \underbrace{4096}_{\text{features.15}} + \underbrace{1000}_{\text{avgpool}} \\ & + \underbrace{4096}_{\text{classifier.4}} + \underbrace{1000}_{\text{classifier.6}} \\ = & 1539560 \end{aligned} $	$ \begin{aligned} & 200704 + 200704 + 100352 \\ & + \underbrace{50176}_{\text{maxpool}} + \underbrace{512}_{\text{layer1}} + \underbrace{1000}_{\text{layer2}} \\ = & 553448 \end{aligned} $
rbssc	$(1 + 3 + 9 \cdot 10) \cdot 50 \cdot 1000 = 4700000$	$(1 + 3 + 9 \cdot 10) \cdot 10 \cdot 1000 = 940000$	$(1 + 3 + 9 \cdot 10) \cdot 50 \cdot 1000 = 4700000$
sitv	$(A_1) 2^{16} \cdot (2 \cdot 8 + 2) = 1179648$ $(A_2) 2^{16} \cdot (2 \cdot 10 + 2) = 1441792$	$2^{14} \cdot (2 \cdot 8 + 2) = 294912$ $2^{14} \cdot (2 \cdot 10 + 2) = 360448$	$2^{16} \cdot (2 \cdot 8 + 2) = 1179648$ $2^{16} \cdot (2 \cdot 10 + 2) = 1441792$
si	$(A_1) 2^{17} \cdot (2 \cdot 8 + 2) = 2359296$ $(A_2) 2^{17} \cdot (2 \cdot 10 + 2) = 2883584$	$2^{15} \cdot (2 \cdot 8 + 2) = 589824$ $2^{15} \cdot (2 \cdot 10 + 2) = 720896$	$2^{17} \cdot (2 \cdot 8 + 2) = 2359296$ $2^{17} \cdot (2 \cdot 10 + 2) = 2883584$
shptv	$(A_1) 2^{18} = 262144$ $(A_2) 2^{18} = 262144$	$2^{18} = 262144$ $2^{18} = 262144$	$2^{18} = 262144$ $2^{18} = 262144$
shpv	$(A_1) 2^8 \cdot 15 \cdot 2^6 \cdot 2^4 = 3932160$ $(A_2) 2^8 \cdot 20 \cdot 2^6 \cdot 2^4 = 5242880$	$2^7 \cdot 15 \cdot 2^5 \cdot 2^3 = 491520$ $2^7 \cdot 20 \cdot 2^5 \cdot 2^3 = 655360$	$2^8 \cdot 15 \cdot 2^6 \cdot 2^3 = 1966080$ $2^8 \cdot 20 \cdot 2^6 \cdot 2^3 = 2621440$

Table A.3: Details of the third experimental series: number of activations (summed over all standalone segments; global) and number of samples for each unit per experiment. Sampling scheme 1: means and variances (*sitv*), Sobol indices (*si*); sampling scheme 2: Shapley values (*shpv*).

	AlexNet	ResNet18
Num. activations	$ \begin{aligned} & \underbrace{20412}_{\text{features.2}} + \underbrace{591408}_{\text{features.5}} + \underbrace{5218304}_{\text{features.7}} \\ & + \underbrace{4415488}_{\text{features.9}} + \underbrace{3636}_{\text{avgpool}} \\ & = 10249248 \end{aligned} $	$ \begin{aligned} & \underbrace{134848}_{\text{maxpool}} + \underbrace{2157568}_{\text{layer1}} + \underbrace{815360}_{\text{layer2}} \\ & + \underbrace{1931776}_{\text{layer3}} \\ & = 5039552 \end{aligned} $
Samples / activation	$ \begin{aligned} \text{sitv/si } (A_1) \quad & 2^{13} \cdot (2 \cdot 8 + 2) = 147456 \\ (A_2) \quad & 2^{13} \cdot (2 \cdot 10 + 2) = 180224 \\ \text{shpv } (A_1) \quad & 2^7 \cdot 15 \cdot 2^3 \cdot 2^3 = 122880 \\ (A_2) \quad & 2^7 \cdot 20 \cdot 2^3 \cdot 2^3 = 163840 \end{aligned} $	$ \begin{aligned} & 2^{13} \cdot (2 \cdot 8 + 2) = 147456 \\ & 2^{13} \cdot (2 \cdot 10 + 2) = 180224 \\ & 2^7 \cdot 15 \cdot 2^3 \cdot 2^3 = 122880 \\ & 2^7 \cdot 20 \cdot 2^3 \cdot 2^3 = 163840 \end{aligned} $

Appendix B. Linear discriminant analysis (LDA) of the convolutional sensitivity maps

Predictions of the SA variables share several common trends for all networks. Overall accuracies for VGG11 and AlexNet-Places365 tend to form correspondingly higher and lower values, forming the range within which others' accuracy curves are located. Total Sobol indices' curves tend to be grouped according to the underlying architecture; first-order Sobol ones are less prominent in that sense, and the Shapley values mix AlexNet's and ResNet18's curves. As checkpoints progress deeper, the overall accuracies tend to decrease, and there are trend-breaking checkpoints (features.9, AlexNet; features.10/features.15, VGG11; layer3, ResNet18). Shapley values preserve higher overall accuracy values, while they decrease more rapidly in the case of both Sobol indices.

Single-variable accuracy patterns are similar for all networks. Erasing, rolling and class variables tend to be the most separable (high accuracy) on the first augmentation set. On the second augmentation set the most discriminative variables are horizontal flip, rotation, class and partition for Shapley values, and elliptic local blur and class for both Sobol indices. Interestingly, networks tend to be grouped by their architecture and by the dataset in terms of RMS of single-variable accuracies. Even AlexNet trained on Places365 containing many sleeping neurons is closer to either AlexNet trained on ILSVRC than to other networks (Sobol indices) or ResNet18 trained on Places365 dataset (Shapley values). AlexNet-ILSVRC pair is best matching for ResNet18-ILSVRC pair (Shapley) and AlexNet-Places365 (total Sobol). ResNet18 prefers its own architecture on both datasets. VGG11 is intermediate - as measured by Shapley values, its patterns appear closer to AlexNet's on the same dataset, by Sobol indices - to ResNet18's.

All networks show similar dependencies on confounding with other variables for Shapley values. Class and partition are mutually tangled, and sharpening, grayscaling, Gaussian blurring and adjusting brightness, contrast, saturation tend to be predicted instead of permutation. The permutation itself notably draws out the predictions of sharpness and elliptic local blur variables, as well as colour transforms. In general, permutation is confused with almost all augmentations except rolling, where class and partition are more prominent, horizontal flip, which is slightly displaced by hue, and rotation, in which predictions the horizontal flip and hue are occurring. Colour augmentations from the second augmentation set tend to be mutually mispredicted. In addition to permutation, predictions of erasing lose their scores due to Gaussian blur, grayscale, sharpness variables; grayscale - due to sharpness, Gaussian blur; Gaussian blur - grayscale, sharpness, partially erasing.

The case of Sobol indices earlier produces more uniform confusion values, preventing the specific pairs from being identified.

Appendix C. Hierarchical clustering analysis (HCA) of the damaged predictions

By masking activations during the inference and measuring the corresponding accuracies, we obtained prediction patterns, used as a feature space for further correlation analysis. In order to enhance such analysis,

we additionally performed the hierarchical clustering procedure, which requires extracting the distances between variables of interest (Figures S7.5.1 (a)–(c), S7.5.2 (a)–(b)). Computed correlation matrices can be transformed into distance matrices by applying the following transform: $\tau(\rho) = \sqrt{1 - |\rho|}$, where ρ is a correlation coefficient. HCA has been performed using the hierarchical agglomerative clustering algorithm with average linkage.

In the case of total Sobol indices, the initial distances between single-sample clusters are minimal on the ILSVRC dataset, and it is difficult to match many of them for the first few merges. Thus, we restrict the further analysis by the first-order Sobol indices and Shapley values. Pairs with the same masking SA variable tend to group together (especially for ResNet18), which may be explained by a more considerable impact of guided damaging on the inference in comparison with augmentations of input.

Well-matched augmentations and masks of the same variable from the first augmentation set A_1 (Gaussian blur, grayscale, and erasing, AlexNet; erasing, grayscale, and rolling, VGG11) retain themselves as one-element clusters or ones of a small number of elements until the large-scale merging. For the second augmentation set A_2 , all networks tend to early form clusters which include colour adjustment pairs. These maskings tend to be grouped but are entangled in a non-uniform way, so there is no exact subtrees among either networks or sensitivity values.

Appendix D. Selection of the threshold for single-class sensitivity analysis

To isolate the mean Jaccard values for further analysis, we may search for their statistical outliers. The corresponding probabilistic model can be identified as one related to the problem of sampling n balls from two identical boxes with N unique balls in each. The single Jaccard index corresponds to $f(k) = k/(2n - k)$ as a function of k , that is, the size of the intersection of two n -ball samples, distributed as

$$p(k) = \frac{\binom{n}{k} \binom{N-n}{n-k}}{\binom{N}{n}}, \quad k = \overline{0, n}. \quad (\text{D.1})$$

In other words, k has a hypergeometric distribution with parameters (N, n, n) , with N equal to the total number of classes, n - the number of the most probable classes in a single prediction (top-n). Average value is computed among $s \cdot N$ samples, where s is the number of samples per class. Monte-Carlo method of 10^7 trials provides us with the following estimates: (1) $N = 1000$, $s = 50$, $n = 5$: $q_1 \approx 0.00273$, $q_3 \approx 0.00284$; (2) $N = 365$, $s = 100$, $n = 5$: $q_1 \approx 0.00755$, $q_3 \approx 0.00775$. Thus, the upper thresholds based on the inter-quantile range, $\tau = q_3 + 3/2 \cdot (q_3 - q_1)$, are: $\tau \approx 0.003$ for the ILSVRC dataset, and $\tau \approx 0.0081$ for Places 365.

Computed thresholds were used to highlight the sufficiently high mean Jaccard indices listed in Tables 5, S7.6.1, S7.6.2. Corresponding outlier detection results are also summarized as Table D.4.

Appendix E. Detailed single-class sensitivity analysis

We propose the single-class sensitivity analysis based on the class-sensitivity levels of classifying layers (Tables 2–4), with respect to the statistically confirmed outliers listed in the Table D.4. SA variables selected for our study can be grouped in the following way: colour adjustments (hue, contrast, saturation, brightness, grayscale), local area distortions (erasing, elliptic local blur), global area distortion (Gaussian blurring, sharpness adjustment) and motions (rolling, horizontal flip, rotation). For classes sensitive to motion augmentations, it is natural to expect the presence of symmetry, either vertical line one (horizontal flip), vertical and horizontal line patterns (rolling), or circular (rotation). In the case of local area distortions, the sensitive classes are expected to have discriminative features such as elliptic forms in the frame centre (elliptic local blur), along with filled rectangular areas (erasing). As a global transform, sharpening eliminates blurring, sometimes introducing a sand texture pattern and emphasizing contours and shapes, potentially the most important features for predicting classes sensitive in that sense, and vice versa for Gaussian blurring. While matching class sensitivity with colour adjustments, it is crucial to recognize how they affect the input,

Table D.4: Summarized statistical evaluation of the outliers detected among all mean Jaccard indices. We refer to the corresponding tables and the number of outliers among all considered thresholds, as well as whether masking with raw or inverted sensitivity values (specified within square brackets) were confirmed as delivering non-typical prediction bias.

Part A. Augmentation set 1.

Model	Sens.val.	Erasing	Sharp.	Augmentation	Grayscale	Gaus.blur
<i>ILSVRC</i>						
AlexNet	Sobol	Table 5 [5/5], S7.6.1 (c) [inv.]	—	S7.6.1 (a) [1/5], (b) [2/5]	Table 5 [3/5]	—
	Shapley	S7.6.1 (d) [5/5], (e) [2/5]	S7.6.1 (c) [inv.], (d) [5/5], (e) [5/5], (f) [4/5]	S7.6.1 (c) [inv.]	—	S7.6.1 (d) [2/5], (e) [1/5]
VGG11	Sobol	—	Table 5 [5/5], S7.6.1 (a) [4/5], (b) [5/5], (c) [inv.]	S7.6.1 (a) [3/5], (b) [5/5]	Table 5 [4/5], S7.6.1 (a) [1/5]	Table 5 [1/5], S7.6.1 (a) [1/5]
	Shapley	S7.6.1 (d) [3/5], (e) [4/5]	—	—	—	—
ResNet18	Sobol	Table 5 [4/5], S7.6.1 (c) [inv.]	—	S7.6.1 (a) [1/5]	Table 5 [5/5]	—
	Shapley	—	S7.6.1 (d) [2/5]	—	S7.6.1 (d) [1/5], (f) [2/5]	S7.6.1 (f) [3/5]
<i>Places 365</i>						
AlexNet	Sobol	Table 5 [5/5], S7.6.2 (c) [inv.]	—	Table 5 [1/5], S7.6.2 (a) [1/5]	Table 5 [5/5], S7.6.2 (a) [2/5], (b) [5/5], (c) [inv.]	Table 5 [3/5]
	Shapley	S7.6.2 (d) [3/5], (e) [5/5]	S7.6.2 (c) [raw], (e) [3/5], (f) [3/5]	S7.6.2 (d) [3/5], (e) [5/5]	S7.6.2 (c) [raw]	S7.6.2 (d) [2/5], (e) [2/5]
ResNet18	Sobol	Table 5 [5/5], S7.6.2 (c) [inv.]	Table 5 [5/5], S7.6.2 (b) [1/5], (c) [inv.]	Table 5 [1/5], S7.6.2 (a) [2/5], (b) [5/5], (c) [inv.]	—	Table 5 [4/5]
	Shapley	—	—	S7.6.2 (d) [1/5], (e) [3/5]	S7.6.2 (d) [1/5], (f) [5/5]	S7.6.2 (c) [inv.], (d) [3/5], (e) [5/5], (f) [5/5]

Part B. Augmentation set 2.

Dataset	Model	Bright.	Contrast.	Satur.	Augmentation	Rotation	El.loc.blur
<i>ILSVRC</i>							
AlexNet	Sobol	—	Table 5 [5/5], S7.6.1 (a) [5/5], (b) [4/5]	Table 5 [5/5], S7.6.1 (c) [inv.]	Table 5 [2/5], S7.6.1 (a) [1/5], (b) [5/5], (c) [inv.]	S7.6.1 (a) [1/5], (b) [4/5], (c) [inv.]	Table 5 [3/5], S7.6.1 (a) [4/5]
	Shapley	—	S7.6.1 (c) [inv.], (d) [4/5], (e) [5/5], (f) [4/5], (g) [5/5]	S7.6.1 (d) [5/5], —	—	S7.6.1 (f) [4/5]	—
VGG11	Sobol	S7.6.1 (a) [5/5], (b) [5/5]	Table 5 [5/5], S7.6.1 (a) [2/5], (c) [raw]	Table 5 [5/5], S7.6.1 (a) [5/5], (b) [5/5], (c) [inv.]	S7.6.1 (a) [5/5], (b) [4/5]	Table 5 [2/5], S7.6.1 (a) [3/5], (b) [1/5], (c) [5/5], (d) [inv.]	S7.6.1 (a) [4/5], (b) [1/5]
	Shapley	S7.6.1 (c) [inv.], (e) [2/5], (f) [5/5]	S7.6.1 (d) [5/5], (e) [2/5]	S7.6.1 (f) [3/5]	S7.6.1 (d) [5/5]	S7.6.1 (c) [raw], (e) [1/5]	S7.6.1 (d) [5/5]
ResNet18	Sobol	—	Table 5 [5/5], S7.6.1 (a) [1/5], (b) [4/5], (c) [inv.]	Table 5 [5/5], S7.6.1 (b) [1/5]	Table 5 [5/5], S7.6.1 (b) [1/5], (c) [inv.]	—	Table 5 [3/5], S7.6.1 (a) [2/5], (b) [3/5], (c) [inv.]
	Shapley	S7.6.1 (c) [inv.], (d) [2/5], (e) [3/5], (f) [5/5]	S7.6.1 (c) [inv.]	S7.6.1 (e) [1/5]	—	S7.6.1 (d) [1/5], (e) [3/5]	S7.6.1 (f) [4/5]
<i>Places 365</i>							
AlexNet	Sobol	Table 5 [5/5], S7.6.2 (b) [1/5], (c) [inv.]	Table 5 [5/5], S7.6.2 (a) [1/5], (b) [1/5], (c) [inv.]	Table 5 [5/5], S7.6.2 (c) [inv.]	Table 5 [5/5], S7.6.2 (c) [inv.]	S7.6.2 (a) [4/5], (b) [4/5], (c) [inv.]	Table 5 [2/5]
	Shapley	S7.6.2 (c) [inv.], (d) [3/5], (e) [2/5], (f) [5/5]	—	S7.6.2 (d) [2/5], (e) [5/5]	S7.6.2 (c) [raw], (d) [1/5], (e) [3/5], (f) [5/5]	S7.6.2 (c) [inv.], (d) [1/5], (f) [1/5]	—
ResNet18	Sobol	S7.6.2 (a) [1/5], (b) [3/5]	S7.6.2 (a) [4/5], (b) [5/5], (c) [inv.]	Table 5 [5/5], S7.6.2 (b) [3/5], (c) [inv.]	Table 5 [5/5], S7.6.2 (c) [inv.]	S7.6.2 (a) [4/5], (b) [4/5], (c) [inv.]	S7.6.2 (a) [1/5], (b) [1/5]
	Shapley	S7.6.2 (c) [inv.], (e) [1/5]	—	—	—	S7.6.2 (d) [2/5], (e) [4/5]	—

which may be visualized by changes in colour histograms (channel-wise distributions of intensity values). By adjusting the brightness, one is moving the histogram as a whole towards a left or right edge. The hue adjustment shifts histograms against each other, changing the key colour of the whole image. The contrast adjustment increases (decreases) their variances, highlighting (suppressing) the borders between areas of different colours. The saturation parameter controls the image colourfulness by pulling the histograms apart or pushing them together. The limit case for the latter is a grayscale transform where all histograms coincide in the shared area.

Let us start our analysis with the motion augmentations. Several classes identified as sensitive to the rolling transform barely satisfy the expectations (*indigo bird, soft-coated wheaten terrier*, AlexNet, ILSVRC; *mashed potato, chocolate sauce*, ResNet18, ILSVRC). A clue to comprehend the matter resides within the subset of samples, which includes the framed pictures, either emerged naturally (e.g., *throne room, galley* for AlexNet, Sobol, Places365) or artificially generated. The observation is consistent across all networks and datasets, although the pattern is not limited to these selections, indicating that the sensitivity ranking depends on a concrete learning outcome rather than solely on a dataset.

High prediction bias supporting the class sensitivity to rotation was detected for all considered network-dataset pairs. As expected, classes with object or frame circular symmetry were encountered (ILSVRC: *mushroom, hotpot, facepowder*, partially *paddlewheel, tray, and bathtub*), but most samples of identified classes are footage from a tilted camera or containing objects captured from different angles (ILSVRC: *shoji, abacus, buckle, bathtub, cellular phone*; Places365: *office, home office*), as well as related to the animals photographed in various poses (ILSVRC: *coyote, hyena, weasel, platypus*).

For the horizontal flip, the following common Sobol-sensitive ILSVRC classes were top-scored for two networks, AlexNet and VGG11: *snowmobile, shield, missile*. For the latter two classes, the vertical elongated pattern can be traced, as well as for several Places365 classes (*basement, staircase, forest road, general store indoor, trench*). The *cliff dwelling* (ILSVRC) objects are aligned with the natural landscape and can hardly be distinguished from their flipped copies. The same reasoning partially applies to the other ILSVRC classes (*snowmobile, giant schnauzer, moped, Siberian husky*), whose objects are captured mainly from the side. From another point of view, the latter ones are rather asymmetrical, like several sensitive Places365 classes (*japanese garden, hospital room, cottage, market outdoor*), admitting us to assume that horizontal flip sensitivity is tied to frame symmetry. Since there are also two kinds of individual sensitivity maps of horizontal flip, - sensitive either to the symmetry axis or to the rest field of view, the final-layer sensitivity may be related to both symmetrical and asymmetrical patterns. I.e., the classes are ranked with respect to not only their static inherent properties but also a kind of invariance under the applied transform and its violation.

The next group of augmentations refers to local distortions. The most notable result is the erasing-sensitivity for AlexNet on both datasets (Sobol, Table 5), where the corresponding objects are rectangular screens and monitors (ILSVRC: *screen, monitor, television*; Places365: *home theater, movie theater indoor, television room*) or rectangular-shaped ones (*lighter, pedestal; phone booth, barndoors*). Similar findings are valid for the ResNet18: Sobol indices top-ranked the same *screen, monitor, television* and *home theater, movie theater indoor, television room* classes, along with rectangular-shaped *wardrobe* and *barndoors*. At the same time, it is hard to consistently interpret the classes highlighted by Shapley values (AlexNet, VGG11), as most of them lack filled rectangular patterns. Probably the more abstract pattern of any large filled monochrome or low-colored areas partially blocking the frame view comes to the forefront. Elliptic local blur sensitivity can be explained by matching the shape and position of specific discriminative details in the frame. For AlexNet, (ILSVRC, Sobol)

golf cart and *sports car* objects have round lights or wheel often centred in the frame, *cup* images in several angles appear containing an elliptic-like region, *black and gold garden spider* class contains contrast near-elliptical regions which are important for their recognition; (Places365, Shapley) - *galley* and *kitchen* samples contain rounded metal sinks or kettles, *entrance hall* - many rounded arches, *general store indoor* - circled spots of light on the glass bottles. As for ResNet18, (ILSVRC, Sobol): *lacewing fly* objects have translucent wings of the similar shape, *cleaver* and *stingray* are also shaped alike and contain round spots; (Places365, Sobol): *lecture room* - subset of samples contains microphones with a head of similar shape, *youth hostel* - lamps with rounded lampshades, *greenhouse indoor* - rounded plots and planters. Similar reasoning

may be applied to sensitive classes of VGG11 (Sobol): *barrel, cask* - several objects either have a circular hole in the centre or are captured from the top, *parking meter* - also contain a round filled pattern, *coyote* - in many pictures the animal is filmed from a distance, occupying a small part in the centre, intersecting with the distortion area, *cornet* - certain images capture glaring musical instruments facing the bells; (Shapley): *scabbard* - many short metal daggers, partially resembling the elliptic shape, *computer mouse, mosque* (the main dome) and *wreck* - shape similar to the distortion. However, it is difficult to follow the same logic to interpret some other classes, e.g., *cliff dwelling*, as sensitive to this augmentation.

But the VGG11 is also sensitive to *cliff dwelling* in the context of colour adjustments (contrast, saturation, hue; Sobol). This class is represented by pictures of cliffs, canyons, and stone dwellings in the highland area, and many of these objects are exposed to direct sunlight. Some of these photos have been taken from shade, some from the air. Thus, there is a contrast of light and shade and a prevalence of mono-coloured areas (brown tones, occasionally diluted by green grass and blue sky).

Two networks, ResNet18 (Sobol) and VGG11 (Sobol and Shapley), showed the sensitivity of the *jigsaw puzzle* class to the contrast adjustment. The images of this class are characterized by the bright colours of the puzzle picture and the sharp edges of its pieces, and the contrast tuning influences the visibility of these edges. Similar logic may explain that the following classes were listed as contrast-sensitive: *walking stick, red-breasted merganser, pay-phone, chain* (AlexNet, Sobol, ILSVRC); *parking meter, gyromitra, waffle iron* (VGG11, Shapley); *cornet, shovel* (VGG11, Sobol); *bubble, spotlight, hook/claw* (ResNet18, Sobol, ILSVRC); *drumstick, wing, holster* (ResNet18, Shapley, ILSVRC). In addition, sensitivity to contrast may be attributed to lighting conditions or color palette affecting the boundary visibility of the key scene objects (AlexNet, Sobol, Places365: *television studio, music studio, childs room, amusement arcade, stage indoor*; ResNet18, Sobol, Places365: *desert vegetation, television studio, kindergarden classroom*; AlexNet, Shapley, ILSVRC: *napkin, pig, African crocodile*).

Unlike the previous augmentation, saturation impacts the spacing between channel-wise pixel intensity histograms. The corresponding sensitive classes were identified for almost all networks (except ResNet18, Places 365, Shapley) and share the following basic patterns: there are traces of image processing visible in several samples (e.g., *hay, bubble*); respective objects contain long mono-coloured patches (*refrigerator, upright piano, screen, water bottle, dough*) or distinctive monochrome elements (*holster, wardrobe, archaeological excavation, trench, rotisserie*); respective objects are set against large monochrome elements of the scene (*barbell, sea urchin*); monochrome illumination of the scene or dominating palette of limited colors (*discotheque, ice shelf, stage indoor, ice floe, wet bar*).

Interestingly, the classes sensitive to grayscale transformation differ from the ones for saturation. One is presented in the top-5 list for all three networks, the *tree frog* class (Sobol, ILSVRC). The corresponding images are mainly in green tones, so the inference seems non-reliant on the colour feature. The latter characteristic is essential for several other similar classes: *warthog, scuba diver, Russian wolfhound* - VGG11, Sobol; *chain* - ResNet18, Sobol, ILSVRC; *lakeside* - ResNet18, Shapley, ILSVRC; *mountain path, lawn, sandbox* - AlexNet, Shapley, Places 365. Similarly, the shape seems to be more important for predicting *sweatshirt, lifeboat* (ResNet18, Sobol, ILSVRC); *coral reef, wig* (ResNet18, Shapley, ILSVRC), and several other classes. Another possible factor is the presence of grayscale and sepia images among samples (*hospital room, archive, music studio, coffee shop, physics laboratory* - AlexNet, Sobol, Places 365).

As for hue-sensitive classes, two major patterns related to the key-colour and palette changes can be observed. The samples of the first kind contain the dominant colour of the background with shade varying - including the variability caused by artificial illumination or differences in the natural light level (e.g., *agaric, missile, Chihuahua, house finch, salamandra, breastplate, bee* - ILSVRC; *stage indoor, rainforest, ruin, beer hall, plaza, discotheque* - Places365). The second recognizable pattern emphasizes the colour of the key object or its critical feature, especially for close-up shots (*digital clock, botanical garden, vegetable garden, florist shop indoor*). Several hue-sensitive classes combine both patterns (*slum, jeep, jellyfish, recreation room*).

Similarly, one may isolate the following pair of typical patterns for brightness-sensitive classes: rich colorful content (*grey wolf, howler monkey, bookshop* - ILSVRC; *childs room, playroom, candy store, art studio, pizzeria, bazaar indoor* - Places365); various luminosity levels, often lighting-dependent (*worm fence, boxer, cliff/drop, creek, patio, crosswalk, rock arch, corral*); their combination (*pinwheel, plate, king snake*;

general store outdoor).

The latter group of augmentations consists of Gaussian blur and sharpness adjustment, both impacting the same high-level image feature, sharpness. Gaussian blur cuts off fine details, complicating the class discrimination. Such fine-detailed classes sensitive to blurring are: *throne room, temple asia, server room* (Places365). Similarly to them, several other classes include low resolution samples (*broom, hair slide - ILSVRC; restaurant, market indoor, children room, shoe shop, kitchen, coffee shop, playroom - Places365*). Others contain defocused or blurred samples (*scuba diver, bubble, green snake - ILSVRC*). Finally, the sensitivity may be due to the inherent coarse properties of the objects (*mask, coho salmon, flat-coated retriever, affenpinscher, dingo; shed, barndoors, driveway, basement, fabric store*).

Sharpness adjustment may introduce a sandy texture or amplify grain artifacts. Several classes identified as sensitive to this augmentation possess similar patterns (*warthog, coho salmon, Alaskan malamute, poncho, harvester/reaper, face powder; excavation, lawn*). There are other classes with fine details, as for blurring augmentation, and images of these classes are frequently diverse, colourful, with numerous details, and are prone to being confused with other classes where similar details emerged due to the augmentation artifacts (*church; delicatessen, bazaar outdoor, church outdoor, temple asia*). Other sensitive classes feature various ripples and edges which the transformation emphasizes (*banister, bee eater, leaf beetle, overskirt, carton, Windsor tie, grasshopper; harbor, elevator lobby*).

References

- [1] G. Levi, T. Hassner, Age and gender classification using convolutional neural networks, in: Proceedings of the IEEE conference on computer vision and pattern recognition workshops, 2015, pp. 34–42.
- [2] D. Wang, Z. Shen, J. Shao, W. Zhang, X. Xue, Z. Zhang, Multiple granularity descriptors for fine-grained categorization, in: Proceedings of the IEEE International Conference on Computer Vision (ICCV), 2015.
- [3] S. Ren, K. He, R. Girshick, J. Sun, Faster R-CNN: Towards real-time object detection with region proposal networks, *IEEE transactions on pattern analysis and machine intelligence* 39 (2016) 1137–1149.
- [4] T. Falk, D. Mai, R. Bensch, Ö. Çiçek, A. Abdulkadir, Y. Marrakchi, A. Böhm, J. Deubner, Z. Jäckel, K. Seiwald, et al., U-Net: Deep learning for cell counting, detection, and morphometry, *Nature methods* 16 (2019) 67–70.
- [5] A. Sadeghian, A. Alahi, S. Savarese, Tracking the untrackable: Learning to track multiple cues with long-term dependencies, in: Proceedings of the IEEE International Conference on Computer Vision (ICCV), 2017.
- [6] Z. Bai, X.-L. Zhang, Speaker recognition based on deep learning: An overview, *Neural Networks* (2021).
- [7] Y. Ren, Y. Ruan, X. Tan, T. Qin, S. Zhao, Z. Zhao, T.-Y. Liu, FastSpeech: Fast, robust and controllable text to speech, in: *NeurIPS* 2019, 2019.
- [8] H. Akbari, L. Yuan, R. Qian, W.-H. Chuang, S.-F. Chang, Y. Cui, B. Gong, VATT: Transformers for multimodal self-supervised learning from raw video, audio and text, *Advances in Neural Information Processing Systems* 34 (2021) 24206–24221.
- [9] B. Rim, N.-J. Sung, S. Min, M. Hong, Deep learning in physiological signal data: A survey, *Sensors* 20 (2020) 969.
- [10] K. Cho, B. van Merriënboer, C. Gulcehre, D. Bahdanau, F. Bougares, H. Schwenk, Y. Bengio, Learning phrase representations using RNN encoder–decoder for statistical machine translation, in: A. Moschitti, B. Pang, W. Daelemans (Eds.), *Proceedings of the 2014 Conference on Empirical Methods in Natural Language Processing (EMNLP)*, Association for Computational Linguistics, Doha, Qatar, 2014, pp. 1724–1734. doi:[10.3115/v1/D14-1179](https://doi.org/10.3115/v1/D14-1179).
- [11] D. Bahdanau, K. H. Cho, Y. Bengio, Neural machine translation by jointly learning to align and translate, in: *3rd International Conference on Learning Representations, ICLR 2015*, 2015.
- [12] T. Young, D. Hazarika, S. Poria, E. Cambria, Recent trends in deep learning based natural language processing, *IEEE Computational intelligence magazine* 13 (2018) 55–75.
- [13] V. Belle, I. Papantonis, Principles and practice of explainable machine learning, *Frontiers in Big Data* 4 (2021) 39. doi:[10.3389/fdata.2021.688969](https://doi.org/10.3389/fdata.2021.688969).
- [14] P. Linardatos, V. Papastefanopoulos, S. Kotsiantis, Explainable AI: A review of machine learning interpretability methods, *Entropy* 23 (2021) 18.
- [15] D. Erhan, Y. Bengio, A. Courville, P. Vincent, Visualizing higher-layer features of a deep network, University of Montreal 1341 (2009) 1.
- [16] M. D. Zeiler, R. Fergus, Visualizing and understanding convolutional networks, in: *European conference on computer vision*, Springer, 2014, pp. 818–833.
- [17] A. Mahendran, A. Vedaldi, Understanding deep image representations by inverting them, in: *Proceedings of the IEEE conference on computer vision and pattern recognition*, 2015, pp. 5188–5196.
- [18] A. Dosovitskiy, T. Brox, Inverting visual representations with convolutional networks, in: *Proceedings of the IEEE conference on computer vision and pattern recognition*, 2016, pp. 4829–4837.
- [19] D. Bau, B. Zhou, A. Khosla, A. Oliva, A. Torralba, Network dissection: Quantifying interpretability of deep visual representations, in: *Proceedings of the IEEE conference on computer vision and pattern recognition*, 2017, pp. 6541–6549.

[20] Z. Qin, F. Yu, C. Liu, X. Chen, How convolutional neural networks see the world—A survey of convolutional neural network visualization methods, *Mathematical Foundations of Computing* 1 (2018) 149.

[21] Y. Li, G. K. Anumanchipalli, A. Mohamed, P. Chen, L. H. Carney, J. Lu, J. Wu, E. F. Chang, Dissecting neural computations in the human auditory pathway using deep neural networks for speech, *Nature Neuroscience* 26 (2023) 2213–2225.

[22] P. Wei, Z. Lu, J. Song, Variable importance analysis: A comprehensive review, *Reliability Engineering & System Safety* 142 (2015) 399–432.

[23] I. M. Sobol, Global sensitivity indices for nonlinear mathematical models and their Monte Carlo estimates, *Mathematics and computers in simulation* 55 (2001) 271–280.

[24] E. Song, B. L. Nelson, J. Staum, Shapley effects for global sensitivity analysis: Theory and computation, *SIAM/ASA Journal on Uncertainty Quantification* 4 (2016) 1060–1083.

[25] B. Kim, M. Wattenberg, J. Gilmer, C. Cai, J. Wexler, F. Viegas, et al., Interpretability beyond feature attribution: Quantitative testing with concept activation vectors (TCAV), in: *International conference on machine learning*, PMLR, 2018, pp. 2668–2677.

[26] S. M. Lundberg, S.-I. Lee, A unified approach to interpreting model predictions, in: I. Guyon, U. V. Luxburg, S. Bengio, H. Wallach, R. Fergus, S. Vishwanathan, R. Garnett (Eds.), *Advances in Neural Information Processing Systems* 30, Curran Associates, Inc., 2017, pp. 4765–4774.

[27] A. Shrikumar, P. Greenside, A. Kundaje, Learning important features through propagating activation differences, in: *International conference on machine learning*, PMLR, 2017, pp. 3145–3153.

[28] M. T. Ribeiro, S. Singh, C. Guestrin, "Why should I trust you?" Explaining the predictions of any classifier, in: *Proceedings of the 22nd ACM SIGKDD international conference on knowledge discovery and data mining*, 2016, pp. 1135–1144.

[29] V. Petsiuk, A. Das, K. Saenko, Rise: Randomized input sampling for explanation of black-box models, *arXiv preprint arXiv:1806.07421* (2018).

[30] T. Fel, R. Cadene, M. Chalvidal, M. Cord, D. Vigouroux, T. Serre, Look at the variance! Efficient black-box explanations with Sobol-based sensitivity analysis, *Advances in Neural Information Processing Systems* 34 (2021) 26005–26014.

[31] W. Samek, A. Binder, G. Montavon, S. Lapuschkin, K.-R. Müller, Evaluating the visualization of what a deep neural network has learned, *IEEE transactions on neural networks and learning systems* 28 (2016) 2660–2673.

[32] R. Geirhos, C. R. Temme, J. Rauber, H. H. Schütt, M. Bethge, F. A. Wichmann, Generalisation in humans and deep neural networks, *Advances in neural information processing systems* 31 (2018).

[33] D. Hendrycks, T. G. Dietterich, Benchmarking neural network robustness to common corruptions and surface variations, *arXiv preprint arXiv:1807.01697* (2018).

[34] G. Vilone, L. Longo, Notions of explainability and evaluation approaches for explainable artificial intelligence, *Information Fusion* 76 (2021) 89–106.

[35] F. Bachoc, F. Gamboa, M. Halford, J.-M. Loubes, L. Risser, Explaining machine learning models using entropic variable projection, *Information and Inference: A Journal of the IMA* 12 (2023) 1686–1715.

[36] A. Krizhevsky, I. Sutskever, G. E. Hinton, Imagenet classification with deep convolutional neural networks, *Advances in neural information processing systems* 25 (2012) 1097–1105.

[37] K. Simonyan, A. Zisserman, Very deep convolutional networks for large-scale image recognition, *3rd International Conference on Learning Representations (ICLR 2015)* (2015) 1–14.

[38] K. He, X. Zhang, S. Ren, J. Sun, Deep residual learning for image recognition, in: *Proceedings of the IEEE conference on computer vision and pattern recognition*, 2016, pp. 770–778.

[39] D. Purves, G. J. Augustine, D. Fitzpatrick, W. C. Hall, A.-S. LaMantia, R. D. Mooney, M. L. Platt, L. E. White, *Neuroscience*. Sixth Edition, Oxford University Press, 2018.

[40] E. R. Kandel, J. D. Koester, S. H. Mack, S. A. Siegelbaum, *Principles of Neural Science*. Sixth Edition, McGraw Hill, 2021.

[41] G. W. Lindsay, Convolutional neural networks as a model of the visual system: Past, present, and future, *Journal of cognitive neuroscience* 33 (2021) 2017–2031.

[42] M. Gasanov, A. Petrovskaya, A. Nikitin, S. Matveev, P. Tregubova, M. Pukalchik, I. Oseledets, Sensitivity analysis of soil parameters in crop model supported with high-throughput computing, in: *International Conference on Computational Science*, Springer, 2020, pp. 731–741.

[43] W. Hoeffding, A class of statistics with asymptotically normal distribution, *The Annals of Mathematical Statistics* 19 (1948) 293–325.

[44] A. Saltelli, P. Annoni, I. Azzini, F. Campolongo, M. Ratto, S. Tarantola, Variance based sensitivity analysis of model output. Design and estimator for the total sensitivity index, *Computer physics communications* 181 (2010) 259–270.

[45] J. Herman, W. Usher, SALib: An open-source python library for sensitivity analysis, *The Journal of Open Source Software* 2 (2017). doi:[10.21105/joss.00097](https://doi.org/10.21105/joss.00097).

[46] A. Saltelli, Making best use of model evaluations to compute sensitivity indices, *Computer physics communications* 145 (2002) 280–297.

[47] G. Chastaing, F. Gamboa, C. Prieur, Generalized Sobol sensitivity indices for dependent variables: Numerical methods, *Journal of Statistical Computation and Simulation* 85 (2015) 1306–1333.

[48] G. Li, H. Rabitz, P. E. Yelvington, O. O. Oluwole, F. Bacon, C. E. Kolb, J. Schoendorf, Global sensitivity analysis for systems with independent and/or correlated inputs, *The journal of physical chemistry A* 114 (2010) 6022–6032.

[49] R. Ballester-Ripoll, M. Leonelli, Computing Sobol indices in probabilistic graphical models, *Reliability Engineering & System Safety* 225 (2022) 108573.

[50] C. Shorten, T. M. Khoshgoftaar, A survey on image data augmentation for deep learning, *Journal of big data* 6 (2019)

[51] S. Zeki, J. Watson, C. Lueck, K. J. Friston, C. Kennard, R. Frackowiak, A direct demonstration of functional specialization in human visual cortex, *Journal of neuroscience* 11 (1991) 641–649.

[52] H. Ishwaran, J. S. Rao, Spike and slab variable selection: Frequentist and Bayesian strategies, *The Annals of Statistics* 33 (2005) 730–773.

[53] G. Coqueret, Approximate NORTA simulations for virtual sample generation, *Expert Systems with Applications* 73 (2017) 69–81.

[54] B. Zhou, A. Lapedriza, A. Khosla, A. Oliva, A. Torralba, Places: A 10 million image database for scene recognition, *IEEE Transactions on Pattern Analysis and Machine Intelligence* (2017).

[55] L. F. Rossi, K. D. Harris, M. Carandini, Spatial connectivity matches direction selectivity in visual cortex, *Nature* 588 (2020) 648–652.

[56] E. Tring, K. K. Duan, D. L. Ringach, ON/OFF domains shape receptive field structure in mouse visual cortex, *Nature Communications* 13 (2022) 2466.

[57] B. Liang, L. Zhang, G. Barbera, W. Fang, J. Zhang, X. Chen, R. Chen, Y. Li, D.-T. Lin, Distinct and dynamic ON and OFF neural ensembles in the prefrontal cortex code social exploration, *Neuron* 100 (2018) 700–714.

[58] G. R. Yang, M. W. Cole, K. Rajan, How to study the neural mechanisms of multiple tasks, *Current opinion in behavioral sciences* 29 (2019) 134–143.

[59] Conda: A system-level, binary package and environment manager running on all major operating systems and platforms. Computer software. Vers. 2.2.4.0, 2016.

[60] A. Paszke, S. Gross, F. Massa, A. Lerer, J. Bradbury, G. Chanan, T. Killeen, Z. Lin, N. Gimelshein, L. Antiga, A. Desmaison, A. Kopf, E. Yang, Z. DeVito, M. Raison, A. Tejani, S. Chilamkurthy, B. Steiner, L. Fang, J. Bai, S. Chintala, PyTorch: An imperative style, high-performance deep learning library, in: H. Wallach, H. Larochelle, A. Beygelzimer, F. d'Alché-Buc, E. Fox, R. Garnett (Eds.), *Advances in Neural Information Processing Systems* 32, Curran Associates, Inc., 2019, pp. 8024–8035.

[61] A. Collette, *Python and HDF5*, O'Reilly, 2013.

[62] G. Bradski, The OpenCV Library, *Dr. Dobb's Journal of Software Tools* (2000).

[63] C. R. Harris, K. J. Millman, S. J. van der Walt, R. Gommers, P. Virtanen, D. Cournapeau, E. Wieser, J. Taylor, S. Berg, N. J. Smith, R. Kern, M. Picus, S. Hoyer, M. H. van Kerkwijk, M. Brett, A. Haldane, J. F. del Río, M. Wiebe, P. Peterson, P. Gérard-Marchant, K. Sheppard, T. Reddy, W. Weckesser, H. Abbasi, C. Gohlke, T. E. Oliphant, Array programming with NumPy, *Nature* 585 (2020) 357–362. doi:[10.1038/s41586-020-2649-2](https://doi.org/10.1038/s41586-020-2649-2).

[64] P. Virtanen, R. Gommers, T. E. Oliphant, M. Haberland, T. Reddy, D. Cournapeau, E. Burovski, P. Peterson, W. Weckesser, J. Bright, S. J. van der Walt, M. Brett, J. Wilson, K. J. Millman, N. Mayorov, A. R. J. Nelson, E. Jones, R. Kern, E. Larson, C. J. Carey, Í. Polat, Y. Feng, E. W. Moore, J. VanderPlas, D. Laxalde, J. Perktold, R. Cimrman, I. Henriksen, E. A. Quintero, C. R. Harris, A. M. Archibald, A. H. Ribeiro, F. Pedregosa, P. van Mulbregt, SciPy 1.0: Fundamental Algorithms for Scientific Computing in Python, *Nature Methods* 17 (2020) 261–272. doi:[10.1038/s41592-019-0686-2](https://doi.org/10.1038/s41592-019-0686-2).

[65] Wes McKinney, Data Structures for Statistical Computing in Python, in: Stéfan van der Walt, Jarrod Millman (Eds.), *Proceedings of the 9th Python in Science Conference*, 2010, pp. 56 – 61. doi:[10.25080/Majora-92bf1922-00a](https://doi.org/10.25080/Majora-92bf1922-00a).

[66] The pandas development team, pandas-dev/pandas: Pandas, 2020. doi:[10.5281/zenodo.3509134](https://doi.org/10.5281/zenodo.3509134).

[67] F. Pedregosa, G. Varoquaux, A. Gramfort, V. Michel, B. Thirion, O. Grisel, M. Blondel, P. Prettenhofer, R. Weiss, V. Dubourg, J. Vanderplas, A. Passos, D. Cournapeau, M. Brucher, M. Perrot, E. Duchesnay, Scikit-learn: Machine learning in Python, *Journal of Machine Learning Research* 12 (2011) 2825–2830.

[68] M. L. Waskom, seaborn: statistical data visualization, *Journal of Open Source Software* 6 (2021) 3021. doi:[10.21105/joss.03021](https://doi.org/10.21105/joss.03021).

[69] J. D. Hunter, Matplotlib: A 2D graphics environment, *Computing in Science & Engineering* 9 (2007) 90–95. doi:[10.1109/MCSE.2007.55](https://doi.org/10.1109/MCSE.2007.55).

[70] S. Seabold, J. Perktold, statsmodels: Econometric and statistical modeling with python, in: 9th Python in Science Conference, 2010.

[71] T. Kluyver, B. Ragan-Kelley, F. Pérez, B. Granger, M. Bussonnier, J. Frederic, K. Kelley, J. Hamrick, J. Grout, S. Corlay, P. Ivanov, D. Avila, S. Abdalla, C. Willing, Jupyter notebooks – A publishing format for reproducible computational workflows, in: F. Loizides, B. Schmidt (Eds.), *Positioning and Power in Academic Publishing: Players, Agents and Agendas*, IOS Press, 2016, pp. 87 – 90.